

Carrier-Resolved Photo-Hall Effect

Oki Gunawan^{1*}, Seong Ryul Pae², Douglas M. Bishop¹, Yudistira Virgus¹, Jun Hong Noh^{4,5}, Nam Joong Jeon⁴, Yun Seog Lee^{1,3}, Xiaoyan Shao¹, Teodor Todorov¹, David B. Mitzi^{6,7}, Byungha Shin^{2*}

¹IBM T. J. Watson Research Center, P.O. Box 218, Yorktown Heights, NY 10598, USA.

²Dept. Materials Science and Engineering, Korea Advanced Institute of Science and Technology, 291 Daehak-Ro, Yuseong-Gu, Daejeon 34141, Republic of Korea.

³Dept. Mechanical and Aerospace Engineering, Seoul National University, 1 Gwanak-Ro, Gwanak-Gu, Seoul 08826, Republic of Korea.

⁴Div. of Advanced Materials, Korea Research Institute of Chemical Technology, 141 Gajeong-ro, Yuseong-Gu, Daejeon 305-600, Republic of Korea.

⁵School of Civil, Environmental and Architectural Engineering and Green School, Korea University, Seoul 02841, Republic of Korea.

⁶Dept. of Mechanical Engineering and Material Science, Duke University, Durham, NC 27708, USA.

⁷Dept. of Chemistry, Duke University, Durham, NC 27708, USA.

*Corresponding authors: Oki Gunawan:ogunawa@us.ibm.com, Byungha Shin: byungha@kaist.ac.kr

Majority and minority carrier properties such as type, density and mobility represent fundamental yet difficult to access parameters governing semiconductor device performance. Obtaining this information simultaneously under light illumination would unlock many critical parameters vital for optoelectronic devices and solar cells, but this goal has remained elusive. Here, we demonstrate a carrier-resolved photo-Hall technique that rests on a new equation relating hole-electron Hall mobility difference ($\Delta\mu_H$), Hall coefficient (H) and conductivity (σ): $\Delta\mu_H = d(\sigma^2 H)/d\sigma$. This discovery, together with advances in ac-field Hall measurement using a rotating parallel dipole line system, allows us to *unlock a host of critical parameters for both majority and minority carriers such as recombination lifetime, diffusion length and recombination coefficient*. We successfully apply this technique to a variety of solar absorbers, including high-performance lead-iodide-based perovskites. By mapping the Hall data against varying light intensities, unprecedented simultaneous access to these parameters is demonstrated. This information, buried in the photo-Hall measurement^{1,2}, has so far been elusive for 140 years since the original discovery of Hall effect³. Beyond historical significance, the applications of simultaneous majority/minority carrier measurement are broad, including photovoltaics and other optoelectronic devices.

The Hall effect is one of the most important characterization techniques for electronic materials and has become the basis of fundamental advances in condensed matter physics, such as the integer and fractional quantum Hall effect^{4,5}. The technique reveals fundamental information about the majority charge carrier, i.e. its type (P or N), density and mobility. In a solar cell, the majority carrier parameters determine the overall device architecture, width of the depletion region and bulk series resistance. The minority carrier properties, however, determine other key parameters that

directly impact overall device performance, such as recombination lifetime (τ), (minority carrier) diffusion length (L_D) and recombination coefficients (k_n). Unfortunately, the standard Hall measurement only yields majority carrier information. Studies to collect both majority and minority carrier properties for high-performance light absorbing materials have been attempted, but require a wide range of experimental techniques, which typically use different sample configurations and illumination levels, thereby presenting additional complications in the analysis⁶⁻¹⁴ (cf. Supplementary Information (SI) section F and G).

Extraction of reliable carrier information is particularly sought after in the study of organic-inorganic hybrid perovskites, a family of materials garnering intense attention due to fast progress in achieving high performance solar cells—with the current record power conversion efficiency (PCE) of 23.3%¹⁵—as well as promising applications for other optoelectronics devices including light emitting diodes¹⁶ and photodetectors¹⁷. Full understanding of charge transport properties of perovskites will help unveil the operating principles of the high-performance optoelectronic devices, thereby guiding further improvement.

In this work we present a carrier-resolved photo-Hall (CRPH) measurement technique capable of simultaneously extracting both majority and minority carrier mobilities, densities and subsequent derivative parameters (τ , L_D) as a function of light intensity. This technique rests on two key elements: a new equation that yields the majority/minority Hall mobility difference, and a high sensitivity Hall measurement using a parallel dipole line (PDL) ac Hall system (Fig. 1a,b)¹⁸. In the classic Hall measurement without illumination, one can obtain three parameters for majority carriers: the (i) type (P or N), from the sign of Hall coefficient H ; (ii) density ($n_C = r/He$), and (iii) Hall mobility ($\mu_H = \sigma H$), where e is the electron charge, n_C is the carrier density and r is the Hall scattering factor. The key challenge in the photo-Hall transport problem, i.e. to extract the majority and minority carrier information, is to solve for three unknowns at a given illumination level: hole and electron (drift) mobility (μ_P , μ_N) and their photocarrier densities (Δn , Δp), which are equal under steady state conditions. Unfortunately, we only have two measured quantities: σ and H , as a function of illumination. The key insight in solving this problem is illustrated in Fig. 1c. Consider two P -type systems with the same majority carrier density (p_0) and mobility (μ_P) but different minority carrier mobility (μ_N). When these systems are excited with the same photocarrier density, Δn_{max} , they will produce different σ - H curves—due to the increasing role of the minority carrier to the total conductivity—even though they start from the same point in the dark. Therefore, the characteristics of the σ - H curves, specifically the slope ($dH/d\sigma$), contains information about the detailed mobilities of the two systems. We show that the (drift) mobility difference, $\Delta\mu = \mu_P - \mu_N = \Delta\mu_H/r$, with $\Delta\mu_H$ (the Hall mobility difference) is given as (SI B):

$$\Delta\mu_H = \frac{d(\sigma^2 H)}{d\sigma} = \left(2 + \frac{d \ln H}{d \ln \sigma}\right) \sigma H \quad (1)$$

Note that σ and H are experimentally obtained as a function of varying light intensity or photocarrier density Δn , but fortuitously the Δn term cancels out of Eq. 1. There are two equivalent expressions for Eq. 1 where the former and the latter are used for low and high injection level

analysis respectively. The term $d \ln H/d \ln \sigma$ has special experimental meaning, as shown for the perovskite example discussed later. This equation applies to both carrier types and assumes that the dark carrier density (p_0 or n_0) are fixed, $\Delta n = \Delta p$ under steady state condition and the mobilities are constant as a function of light intensity (see SI B.2 for a generalized model where mobilities vary with illumination). The Hall scattering factor r generally lies between 1 and 2. It approaches 1 at high magnetic field and generally is assumed to be 1,¹⁹ including in this report. Using the known two-carrier expressions in the low-magnetic-field regime ($B \ll 1/\mu$)²⁰—i.e., $\sigma = e(p\mu_p + n\mu_n)$ and $H = r(p - \beta^2 n)/(p + \beta n)^2 e$, where p and n are hole and electron densities and $\beta = \mu_n/\mu_p$ is the mobility ratio—we can completely solve the photo-Hall transport problem, e.g. for a *P*-type material:

$$\beta = \frac{2\sigma(r\Delta\mu - \sigma H) - re\Delta\mu^2 p_0 \pm \Delta\mu\sqrt{rep_0}\sqrt{re\Delta\mu^2 p_0 + 4\sigma(\sigma H - r\Delta\mu)}}{2\sigma(r\Delta\mu - \sigma H)} \quad (2)$$

$$\Delta n = \frac{\sigma(1 - \beta) - e\Delta\mu p_0}{e\Delta\mu(1 + \beta)} \quad (3)$$

Finally, we obtain: $\mu_p = \Delta\mu/(1 - \beta)$ and $\mu_n = \beta\mu_p$. Note that we need to know the background hole density, p_0 , from the dark measurement. Eqs. 1-3 are referred to as the " $\Delta\mu$ " calculation model.

The second ingredient enabling the CRPH measurement involves obtaining a clean Hall signal. Unfortunately, in many photovoltaic films, high sample resistance ($R > 10 \text{ G}\Omega$), as in the case for perovskites, or low mobility ($\mu < 1 \text{ cm}^2/\text{Vs}$) can produce noisy Hall signals. Therefore, ac field Hall techniques coupled with Fourier analysis and lock-in detection are crucial. We recently developed a high sensitivity ac-field Hall system based on a rotating PDL magnet system^{18,21,22}. The PDL system is a recently-discovered natural magnetic trap that harbors a new type of field confinement effect that generates a magnetic camelback potential along its longitudinal axis²³. This effect is used to optimize the field uniformity (see SI A). The PDL Hall system consists of a pair of diametric cylindrical magnets separated by a gap. One magnet (the "master") is driven by a motor and another (the "slave") follows in the opposite direction. This system produces a *unidirectional* and *single harmonic field* at the center where the sample resides (see Fig. 1b and Video S1), which forms the basis for a successful photo-Hall experiment. Besides the photo-Hall measurement, optical measurements (e.g., transmission and reflectivity) to calculate the absorbed photon density (G_γ) can also be done in the same setup (Fig. 1a and SI C).

To demonstrate the CPRH technique, two examples are discussed in detail: a lead-halide-based perovskite film and a silicon sample, which serve as high ($\Delta n > p_0$) and low ($\Delta n < p_0$) injection cases, respectively. The first example employs a (FA,MA)Pb(I,Br)₃ (FA=formamidinium, MA=methylammonium) perovskite film, fabricated using the same method that produced a recent record PCE²⁴, but with further process optimization. A companion device in the same batch yielded PCE of 20.8% (see Methods). The measurement device is a Hall bar with sample thickness $d = 0.55 \mu\text{m}$ (Fig. 2b inset). First, we measured the sample in the dark and obtained the majority carrier

properties: *P*-type, $p_0=8.3\times10^{11}/\text{cm}^3$ and $\mu_P=9.8 \text{ cm}^2/\text{Vs}$. Then, we performed the measurements under several laser intensities (wavelength $\lambda=638 \text{ nm}$, up to $\sim40 \text{ mW/cm}^2$). An example of longitudinal (R_{XX}) and transverse (R_{XY}) magnetoresistance under light are shown in Fig. 2a. The R_{XY} trace shows the expected Hall signal with a Fourier component at the same frequency (f_{REF}) as the magnetic field B [Fig. 2a(vii)]. The desired Hall signal R_H is obtained using numerical lock-in detection based on a reference sinusoidal signal with the same phase as B [Fig. 2a(iv)]¹⁸. The σ and H values are then calculated from R_{XX} and R_H . We also observe a second harmonic component at $2f_{\text{REF}}$ in the R_{XY} Fourier spectrum [Fig. 2a(vii)], which is also evident in the original R_{XY} trace as a double frequency oscillation [Fig. 2a(iii)]. This component is not the desired Hall signal and thus is rejected. It arises from another magnetoresistance effect²⁵, which is stronger in R_{XX} [Fig. 2a(ii)]. It also appears in R_{XY} because of R_{XX} - R_{XY} mixing due to the finite size of the Hall bar contact arms. This *highlights the importance* of inspecting the Hall signal's Fourier spectrum and using lock-in detection, as opposed to simple amplitude measurement.

The measurement returns a series of σ and H points that change significantly with illumination (Fig. 2b): σ increases by $\sim340\times$ and H drops by $\sim1400\times$. The new photo-Hall equation (Eq. 1) *provides an astonishingly simple and quick insight into the data* by looking at the slope of the σ - H data using the log scale. If the slope ($d\ln H/d\ln \sigma$) is equal to -2, then $\mu_P=\mu_N$, if it is larger (less) than -2 while H is positive, then $\mu_P>\mu_N$ ($\mu_P<\mu_N$). From Fig. 2b we obtain the overall $d\ln H/d\ln \sigma=-1.36$, which implies that $\mu_P>\mu_N$. Furthermore, we could evaluate $\Delta\mu_H$ at any σ - H point, e.g. at the maximum light intensity: $\Delta\mu_H=1.9 \text{ cm}^2/\text{Vs}$. We proceed to solve for μ_P , μ_N and Δn using the previously discussed " $\Delta\mu$ " model and plot them with respect to G_γ (Fig. 2c). Due to significant change in mobility with light intensity in the perovskite sample, we used the generalized $\Delta\mu$ model as discussed in SI B.2. This model introduces a correction due to varying mobilities as much as $0.5\times$ to the final mobility values at the highest light intensity. We obtain the final solution: $\mu_P=(14-28) \text{ cm}^2/\text{Vs}$ and $\mu_N=(7-26) \text{ cm}^2/\text{Vs}$, which both increase with G_γ . This increase could arise from a light-modulated intragranular barrier effect¹. We further obtained Δn , which increases with G_γ as expected. For comparison, we also plot the "single carrier" Hall mobility ($\mu_H=\sigma H$) and Hall density ($n_H=1/eH$), which are often used to estimate μ and Δn in past photo-Hall studies¹³. As seen in Fig. 2c, these estimates can be very different from the actual μ_P , μ_N and Δn values obtained from the CRPH measurement.

In addition to the basic majority and minority carrier properties, we can now investigate the recombination mechanism with unprecedented detail by studying the Δn vs. G_γ data in Fig. 2c. The data show two power law regimes following $\Delta n \sim G_\gamma^m$ with $m \sim 1$ and $m \sim 0.5$. The $m=1$ ($m=0.5$) behavior is expected for monomolecular recombination (bimolecular recombination) regime¹³, however in this case the $m \sim 0.5$ regime is more likely explained by trapping. Consider for example a single-level trap model. The lifetime, e.g. for hole, is given as: $\tau=1/C_P n_r$, with C_P representing the capture cross section for hole and n_r is the trapped electrons density. At very low light intensities, the lifetime is constant as n_r is dominated by the equilibrium (dark) level of charged electron traps: $n_r=n_{r0}$. As the light intensity increases, the number of charged traps increase due to the increase in injected electrons. This in turn reduces τ and explains the low exponent ($m \sim 0.5$) in Fig. 2c²⁶. The alternative explanation of bimolecular recombination can be discarded since the maximum photocarrier density in our experiment ($\Delta n \sim 10^{14} \text{ /cm}^3$) is $\sim 1000\times$

below the typical density needed ($\Delta n \sim 10^{17}/\text{cm}^3$) for the bimolecular recombination to dominate in perovskite^{27,28} (SI D).

The measurement also provides access to the recombination lifetime, $\tau = \Delta n/G$ and the carrier diffusion length, $L_D = \sqrt{k_B T \mu \tau / e}$, where k_B is the Boltzmann constant and T is temperature. G is the photocarrier generation rate given as: $G = \eta G_\gamma$ where η is the photocarrier generation efficiency which is often assumed to be unity. At high injection level when $\Delta n, \Delta p > p_0$, it is more appropriate to use an ambipolar diffusion length²⁹, which fortunately can also be calculated from our CRPH data: $L_{D,am} = \sqrt{k_B T \tau (n + p) / e (n/\mu_P + p/\mu_N)}$. Furthermore, we can map these results as a function of Δn (Fig. 2d). The hole, electron and ambipolar diffusion lengths fall very close to each other given similar hole/electron mobilities. From this analysis, we obtain τ up to 40 μs and $L_D \sim 30 \mu\text{m}$ at the lowest light intensity; however, they vary drastically, and drop to 44 ns and 1.7 μm at the highest light intensity. The relatively high τ and L_D obtained in this study attest to the high quality of this perovskite film²⁴. We also compare our results with recent transport studies for perovskites in Table S3 and obtain general agreement. We highlight that, given the large variation in τ and L_D with G_γ , noting G_γ or Δn when reporting these measurements is crucial.

In the second example, we present a study employing single crystal silicon. The sample is a Hall bar made of B-doped, Czochralski-grown silicon with active area of 3 mm×3mm and thickness $d=725 \mu\text{m}$. This study provides a useful CRPH demonstration for a well-known material, in the low injection regime and with a large thickness ($d >> 1/\alpha$ and L_D). We used a laser with $\lambda=638 \text{ nm}$ and intensity up to 50 mW/cm². First, we obtain the σ - H curve that begins with positive H value in the dark, indicating a P -type material with $p_0=6.6 \times 10^{12} / \text{cm}^3$ (Fig. 3b). At higher light intensity, H inverts to negative values, indicating increasing electron (minority) carrier conductivity. For convenient $\Delta\mu_H$ extraction we plot $\sigma^2 H$ vs. σ in Fig. 3b inset, which is more appropriate for low injection analysis. The data shows a monotonic behavior with nearly constant slope at high intensity regime, which yields $\Delta\mu_H=-1070 \text{ cm}^2/\text{Vs}$.

We then proceed to calculate μ_P , μ_N and Δn using Eqs. 2 and 3, with results shown in Fig. 3c-d. We obtain average majority mobility, $\mu_P=486 \text{ cm}^2/\text{Vs}$, and minority mobility, $\mu_N=1560 \text{ cm}^2/\text{Vs}$, in good agreement with the known hole ($\sim 500 \text{ cm}^2/\text{Vs}$) and electron ($\sim 1500 \text{ cm}^2/\text{Vs}$) mobility in silicon²⁰. These values are sufficiently constant so that we do not need to attempt the mobility variation correction using the generalized model as discussed in the perovskite analysis. We also obtained a Δn vs. G_γ curve that follows $\Delta n \sim G_\gamma^m$, with $m=1.2$, suggesting monomolecular recombination regime, as expected for silicon (ref. 20, Fig. 7.3). At the highest light intensity, we obtain $\tau \sim 2 \mu\text{s}$ and $L_{D,N} \sim 90 \mu\text{m}$. For comparison, we have also measured the lifetime using quasi-steady-state photoconductance technique³⁰ which yields lifetime of 1-5 μs for $\Delta n = 2 \times 10^{12} - 10^{13} / \text{cm}^3$ in close agreement with the CRPH result (Fig. 3d, cf. Methods). For additional example of CRPH study in the low injection regime, we have also studied another highly interesting solar material, kesterite $\text{Cu}_2\text{ZnSn}(\text{S},\text{Se})_4$ in SI E and G.

In summary, in contrast to the classic Hall effect, which only yields three parameters, the CRPH technique yields $7N$ parameters: μ_P , μ_N , Δn , τ , $L_{D,N}$, $L_{D,P}$ and $L_{D,am}$ repeated at N light intensities. Additionally, one can also calculate the relevant recombination coefficient, e.g. $k_1=1/\tau$ in the

monomolecular recombination regime. Of the dozens of electrical transport measurements performed on perovskites as summarized in Tables S3, this is the first time that all minority and majority carrier characteristics have been determined *simultaneously from a single experimental setup, on a single sample and mapped against varying light intensities under steady state conditions*. This clearly demonstrates the power of this CRPH technique and represents a significant expansion of the Hall measurement after its original discovery in 1879³. The approach should also provide a valuable probe of optoelectronic parameters for a broad range of conventional and emerging semiconductors beyond perovskite.

References:

1. Fowler, A. Photo-Hall effect in CdSe sintered photoconductors. *J. Phys. Chem. Sol.* **22**, 181-188 (1961).
2. Dresner, J. The photo-Hall effect in vitreous selenium. *J. Phys. Chem. Sol.* **25**, 505-511 (1964).
3. Hall, E. H. On a new action of the magnet on electric currents. *Am. J. Math.* **2**, 287-292 (1879).
4. Klitzing, K. v., Dorda, G. & Pepper, M. New method for high-accuracy determination of the fine-structure constant based on quantized Hall resistance. *Phys. Rev. Lett.* **45**, 494-497 (1980).
5. Tsui, D. C., Stormer, H. L. & Gossard, A. C. Two-dimensional magnetotransport in the extreme quantum limit. *Phys. Rev. Lett.* **48**, 1559-1562 (1982).
6. Poncea Jr, C. S. *et al.* Organometal halide perovskite solar cell materials rationalized: ultrafast charge generation, high and microsecond-long balanced mobilities, and slow recombination. *J. Am. Chem. Soc.* **136**, 5189-5192 (2014).
7. Leijtens, T. *et al.* Electronic properties of meso-superstructured and planar organometal halide perovskite films: charge trapping, photodoping, and carrier mobility. *ACS Nano* **8**, 7147-7155 (2014).
8. Xing, G. *et al.* Long-range balanced electron-and hole-transport lengths in organic-inorganic $\text{CH}_3\text{NH}_3\text{PbI}_3$. *Science* **342**, 344-347 (2013).
9. Stranks, S. D. *et al.* Electron-hole diffusion lengths exceeding 1 micrometer in an organometal trihalide perovskite absorber. *Science* **342**, 341-344 (2013).
10. Wehrenfennig, C., Liu, M., Snaith, H. J., Johnston, M. B. & Herz, L. M. Charge-carrier dynamics in vapour-deposited films of the organolead halide perovskite $\text{CH}_3\text{NH}_3\text{PbI}_{3-x}\text{Cl}_x$. *Energy & Environ. Sci.* **7**, 2269 (2014).
11. Shi, D. *et al.* Low trap-state density and long carrier diffusion in organolead trihalide perovskite single crystals. *Science* **347**, 519-522 (2015).
12. Dong, Q. *et al.* Electron-hole diffusion lengths $>175\text{ }\mu\text{m}$ in solution-grown $\text{CH}_3\text{NH}_3\text{PbI}_3$ single crystals. *Science* **347**, 967-970 (2015).
13. Chen, Y. *et al.* Extended carrier lifetimes and diffusion in hybrid perovskites revealed by Hall effect and photoconductivity measurements. *Nat. Comm.* **7**, 12253 (2016).
14. Gokmen, T., Gunawan, O. & Mitzi, D. B. Minority carrier diffusion length extraction in $\text{Cu}_2\text{ZnSn}(\text{Se},\text{S})_4$ solar cells. *J. Appl. Phys.* **114**, 114511 (2013).
15. National Renewable Energy Laboratories, *Best research-cell efficiencies*, <https://www.nrel.gov/pv/assets/pdfs/best-research-cell-efficiencies-190416.pdf> (2019).

16. Tan, Z.-K. *et al.* Bright light-emitting diodes based on organometal halide perovskite. *Nat. Nano.* **9**, 687-692 (2014).
17. Dou, L. *et al.* Solution-processed hybrid perovskite photodetectors with high detectivity. *Nat. Comm.* **5**, 5404 (2014).
18. Gunawan, O., Virgus, Y. & Fai Tai, K. A parallel dipole line system. *Appl. Phys. Lett.* **106**, 062407 (2015).
19. Sze, S. M. & Ng, K. K. *Physics of Semiconductor Devices*. 3rd edn. (John Wiley & Sons, Hoboken, New Jersey, 2006).
20. Schroder, D. K. *Semiconductor Material and Device Characterization*. 3rd edn. (John Wiley & Sons, Inc., Hoboken, New Jersey, 2006).
21. Gunawan, O. & Gokmen, T. Hall measurement system with rotary magnet. US patent 9,041,389 (2015).
22. Gunawan, O. & Pereira, M. Rotating magnetic field Hall measurement system. US patent 9,772,385 (2017).
23. Gunawan, O. & Virgus, Y. The one-dimensional camelback potential in the parallel dipole line trap: Stability conditions and finite size effect. *J. Appl. Phys.* **121**, 133902 (2017).
24. Jeon, N. J. *et al.* Compositional engineering of perovskite materials for high-performance solar cells. *Nature* **517**, 476-480 (2015).
25. Zhang, C. *et al.* Magnetic field effects in hybrid perovskite devices. *Nat. Phys.* **11**, 427-434 (2015).
26. Levine, I. *et al.* Can we use time-resolved measurements to get steady-state transport data for halide perovskites? *J. Appl. Phys.* **124**, 103103 (2018).
27. Wehrenfennig, C., Eperon, G. E., Johnston, M. B., Snaith, H. J. & Herz, L. M. High charge carrier mobilities and lifetimes in organolead trihalide perovskites. *Adv. Mater.* **26**, 1584-1589 (2014).
28. Sum, T. C. *et al.* Spectral features and charge dynamics of lead halide perovskites: origins and interpretations. *Acc. Chem. Res.* **49**, 294-302 (2016).
29. Rosling, M., Bleichner, H., Jonsson, P. & Nordlander, E. The ambipolar diffusion coefficient in silicon: Dependence on excess-carrier concentration and temperature. *J. Appl. Phys.* **76**, 2855-2859 (1994).
30. Sinton, R. A. & Cuevas, A. Contactless determination of current-voltage characteristics and minority carrier lifetimes in semiconductors from quasi steady state photoconductance data. *Appl. Phys. Lett.* **69**, 2510-2512 (1996).

Supplementary Information:

Supplementary Information:

(Section A-H, Figures S1 to S8, Tables S1 to S4, Equations 4 to 38, References 31 to 83)

Animation Video S1

Acknowledgements:

S.R.P. and B.S. thank financial support from the Technology Development Program to Solve Climate Changes of the National Research Foundation (NRF) funded by the Ministry of Science, ICT & Future Planning (No. 2016M1A2A2936757), and from the Korea Institute of Energy Technology Evaluation and Planning (KETEP) and the Ministry of Trade, Industry & Energy (MOTIE) of the Republic of Korea (No. 20173010012980). J.H.N. thanks financial support from NRF grant funded by the Korea government (MSIP) (2017R1A2B2009676, 2017R1A4A1015022). D.B.M. and O.G. thanks National Science Foundation for support under Grant No. DMR-1709294. We thank Supratik Guha for managing the IBM photovoltaics (PV) program, Hendrik Hamann for support, Michael Pereira and Kong Fai Tai for PDL Hall development, Bahman Hekmatshoartabari for the silicon sample and Jekyung Kim for Table S4.

Authors contributions:

O.G. (PI, IBM) and B.S. (PI, KAIST) conceived the project. O.G. led the project, built the experimental setup, programmed the analysis software, derived Eq. 1 and other formulas, performed measurement and analyses. S.R.P. prepared samples, performed optical and Hall measurements and analysis. O.G., S.R.P., B.S. and D.B. developed data analysis, interpretation and participated in manuscript writing. Y.V. helped in PDL system development and formula derivation. Y.S.L. and D.B. helped in optical study. N.J.J. and J.H.N. prepared the perovskite samples and solar cells. D.B.M., T.T. and X.S. developed the champion CZTSSe process, D.B.M. managed the IBM PV program and participated in manuscript writing.

Author Information:

Reprints and permissions information is available at www.nature.com/reprints. Readers are welcome to comment on the online version of the paper. Correspondence should be addressed to: O.G. (ogunawa@us.ibm.com) or B.S. (byungha@kaist.ac.kr).

Competing interest:

The PDL Hall system was developed at IBM Research and documented in the following patent families: (1) O. Gunawan, T. Gokmen, US 9,041,389²¹ (2) O. Gunawan, M. Pereira, US 9,772,385,²² US 9,678,040, US 15/581183 and related foreign patent applications (WO 2016162772A1, UK 1717263.6, Japan 2017-552496, Germany 112016000875.9). (3) O. Gunawan, US 15/281,968. (4) O. Gunawan, W. Zhou, US 16/382,937. Patent (1) and (2) cover the basic ac field/PDL Hall system and (3) and (4) cover the related photo Hall setup and method.

Data availability:

The datasets generated and analyzed during the current study are available from the corresponding author on reasonable request.

Methods:

Photo Hall Measurement

The experimental setup is shown in Fig. 1a. All measurements were performed at room temperature. Photo-excitation was achieved using a solid-state red laser ($\lambda = 638$ nm, max. power 190 mW) for the perovskite and silicon, or a blue laser ($\lambda = 450$ nm, max. power 500 mW) for kesterite (SI E, G). The sample is centered between the PDL magnets and the laser beam is directed through a motorized neutral density filter. A cylindrical lens is used to expand the beam, while a wedge lens deflects the beam onto the sample area. A beam splitter is used to split the beam towards a "Monitor" silicon photodetector (PD) to measure the monitor photocurrent (I_{PD-MON}) at every light intensity. The I_{PD-MON} is used to determine the incident photon flux (Φ) and the absorbed photon density (G_γ) on the sample, which is given as: $G_\gamma = (1-R)\Phi[1-\exp(-\alpha d)]/d$, where R is the reflectivity, α is the absorption coefficient and d is the thickness (SI C). The optical properties of the films studied in this work are presented in Table S2.

The details of the PDL Hall system are described in SI A. The electronic instrumentation consists of a custom-built PDL motor control box, Keithley 2450 source meter unit (SMU) to apply the voltage or current source to the sample, Keithley 2001 digital multi meter (DMM) for voltage measurement, Keithley 7065 Hall switch matrix card with high impedance buffer amplifiers for routing the signals between the samples, SMU and DMM. For samples with relatively high mobility (perovskite and silicon) we use the dc current excitation mode, and for low mobility sample (e.g. kesterite) we use ac current excitation mode with SRS830 lock-in amplifier to achieve better noise rejection. The PD current is measured using a Keithley 617 electrometer.

At every light intensity, the sheet resistance (R_S) is obtained by measuring 2 states and 8 states of longitudinal magnetoresistance (R_{XX}) for six-terminal Hall bar and four-terminal Van der Pauw sample respectively. For the Hall bar sample, the sheet resistance is given as $R_S = R_{XX}W/L$, where W is the width and L is the length of the Hall bar active area. The conductivity of the sample is given as: $\sigma = 1/R_S d$. Next, the transverse magnetoresistance (R_{XY}) is measured. The PDL master magnet is rotated by a stepper motor system, typically with a speed of 1 to 2 rpm, to generate ac field. A typical magnetic field amplitude on the sample is ~ 0.70 T for a PDL magnet gap of ~ 10 mm. A Hall sensor is placed under the master magnet to monitor the oscillating field. The field and R_{XY} are recorded as a function of time for 15 to 30 min each sweep. This measurement is repeated at several light intensities ranging from dark to the brightest level, while recording the "Monitor" PD current to determine G_γ . After all of the measurements are completed, the sample was replaced with a "Reference" photodetector (PD). We then determined the photo current ratio, $k_{PD} = I_{PD-MON}/I_{PD-REF}$, between the Reference PD and the Monitor PD at every given light intensity (see SI C for further detail).

Hall signal analysis is performed using a custom program developed in MATLAB²². Fourier spectral analysis is used to inspect the existence of the magnetoresistance signal (R_{XY}) at the same frequency as the magnetic field. We then proceed with phase sensitive lock-in detection, implemented by software, to extract the in-phase component of the Hall signal (R_H) while rejecting the out-of-phase component that arises from various sources, such as Faraday emf induction. We use a typical lock-in time constant of 120-300 s. The Hall coefficient is calculated using $H = R_H d/B_0$, where B_0 is the magnetic field amplitude. Therefore, at every light intensity, we obtain

a set of σ and H values and proceed with the photo-Hall analysis. We also provide additional CRPH studies for MAPbI_3 perovskite and a kesterite sample in SI E and G. For the alternative lifetime measurement in silicon using quasi-steady-state photoconductance technique we used Sinton Instruments WCT-120³⁰. The measurement was done on the 6" silicon wafer from which the Hall sample originated.

We also make a general remark about the CRPH analysis. First, in the very low light intensity (or low injection) regime, e.g. $G_\gamma < 5 \times 10^{17} \text{ /cm}^3\text{s}$ for the silicon sample in Fig. 3c, the CRPH analysis results become inaccurate, the Δn values are scattered higher than expected from the monomolecular recombination trend. From our experience, in analyzing many samples so far (e.g., perovskite, Si, kesterite), we expect that this could be due to the accuracy limitation of the σ and H measurements. For very low light intensity, typically we cannot resolve Δn values smaller than 1% of p_0 , as shown in Fig. 3c. The best analysis results come from the higher intensity regime, where there is large Δn ($\Delta n \gg p_0/100$) such that significant changes in σ and H are noted, as in the perovskite example. Second, if the mobility values of the systems are very low like in the case of kesterite samples ($\mu_p \sim 1 \text{ cm}^2/\text{Vs}$ and $\mu_N \sim 10 \text{ cm}^2/\text{Vs}$), the Hall coefficient measurement become noisier and this also impacts the accuracy of the analysis.

Perovskite Solar Cell

The perovskite films for photo-Hall study are based on the $(\text{FAPbI}_3)_{1-x}(\text{MAPbBr}_3)_x$ mixed-perovskite system, and employ a halide perovskite composition analogous to that used in a previous record PCE of 17.9% at $x=0.15$ as reported by Korea Research Institute of Chemical Technology²⁴. Afterwards the PCE has been improved by modifying the film deposition method and adjusting x value. We demonstrated high average PCE of 20.8% at $x=0.12$ for a $(\text{FAPbI}_3)_{0.88}(\text{MAPbBr}_3)_{0.12}$ device (FTO/bl-TiO₂/mp-TiO₂/perovskite/PTAA/Au) under 1 sun condition (AM1.5G, 100mW/cm²). Extended Data Fig. 1a shows photocurrent density-voltage (J - V) curves for the $(\text{FAPbI}_3)_{0.88}(\text{MAPbBr}_3)_{0.12}$ device measured by reverse and forward scans with 10 mV voltage steps and 40 ms delay times under AM 1.5G illumination. The device exhibits a short circuit current density (J_{SC}) of 23.3 mA/cm², open circuit voltage (V_{OC}) of 1.13 V, and fill factor (FF) of 80.0% by reverse scan. Slightly decreased FF to 77.8% by forward scan results in average PCE of 20.8%. An external quantum efficiency (EQE) spectrum for the device is represented in Extended Data Fig. 1b, showing a very broad plateau of over 80% between 400 and 750 nm. The histogram of PCE values for 80 cells is shown in Extended Data Fig. 1c.

The J - V curves were measured using a solar simulator (Newport, Oriel Class A, 91195A) with simulated AM1.5G illumination at 100 mW/cm² and a calibrated Si-reference cell certificated by NREL. The system uses a Keithley 2420 source meter for I - V measurement. The measurement was done at 25°C under ambient condition. The devices were pre-illuminated for 30 s under 1 sun condition and the measurement was done in reverse (from 1.5V to -0.2V) and forward (from -0.2 to 1.5V) scan directions. The current density-voltage (J - V) curves for the perovskite devices were measured by masking the active area (0.16 cm² measured using an optical microscope) with a metal mask 0.094 cm² in area. The EQE was measured by a power source (Newport 300W Xenon lamp, 66920) with a monochromator (Newport Cornerstone 260) and a multimeter (Keithley 2001).

Perovskite Solar Cell Fabrication

A 70 nm-thick blocking layer of TiO₂ (bl-TiO₂) was deposited onto an F-doped SnO₂ (FTO, Pilkington, TEC8) substrate by spray pyrolysis using a 10 vol% titanium diisopropoxidebis(acetylacetone) solution in ethanol at 450 °C. A TiO₂ slurry was prepared by diluting TiO₂ pastes (Share Chem Co., SC-HT040) in mixed solvent (2-methoxyethanol:terpineol = 3.5:1 w/w). The 100 nm-thick mesoporous-TiO₂ (mp-TiO₂) was fabricated by spin coating the TiO₂ slurry onto the bl-TiO₂ layer and subsequently calcining at 500 °C for 1 hr in air to remove the organic components. Bis(trifluoromethane) sulfonimide lithium salt was treated onto the mp-TiO₂ layer. Then, the (FAPbI₃)_{0.88}(MAPbBr₃)_{0.12} film was formed using the above-mentioned method. A polytriarylamine (PTAA) (EM index, $M_n = 17500 \text{ g.mol}^{-1}$)/toluene (10 mg/1 mL) solution with an additive of 7.5 μL Li-bis (trifluoro-methanesulfonyl) imide (Li-TFSI)/ acetonitrile (170 mg/1 mL) and 4 μL 4-*tert*-butylpyridine (TBP) was spin-coated on the perovskite layer/mp-TiO₂ /bl-TiO₂ /FTO substrate at 3000 rpm for 30 s.

Perovskite Hall Sample Fabrication

All precursor materials were prepared following previous report²⁴. To form the perovskite thin film based on the (FAPbI₃)_{0.88}(MAPbBr₃)_{0.12} absorber the 1.05 M solution dissolving NH₂CH=NH₂I(FAI) and CH₃NH₃Br(MABr) with PbI₂ and PbBr₂ in *N,N*-dimethyl formamide (DMF) and dimethyl sulfoxide (DMSO) (6:1 v/v) was prepared by stirring at 60°C for 1 hour. Then the solution was coated onto a fused silica substrate heated to 60°C by two consecutive spin-coating steps, at 1000 and 5000 rpm for 5 and 10 s, respectively. During the second spin-coating step, 1 mL ethyl ether was poured onto the substrate after 5 s. Then, the substrate was heat-treated at 150°C for 10 min. The compact (FAPbI₃)_{0.88}(MAPbBr₃)_{0.12} film with a thickness of 550 nm was obtained. Then, we selectively scraped the film off the substrate to pattern with the desired Hall bar configuration for photo-Hall measurement. The Hall bar is a six-terminal device (Fig. 2b, inset) with active area of $W \times L = 2 \text{ mm} \times 4 \text{ mm}$. We deposited an Au metal contact pattern (100 nm thick) and installed a header pin to mount the sample to the PDL Hall tool.

Main Figure Legends:

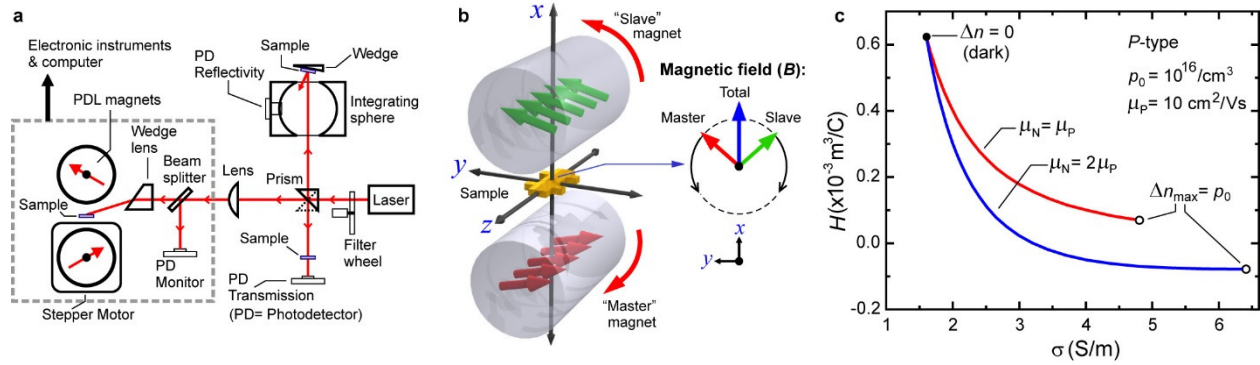


Figure 1. The carrier-resolved photo Hall measurement: (a) The parallel dipole line (PDL) photo Hall setup for a complete photo-Hall experiment. (b) The rotating PDL magnet system that generates a unidirectional and single harmonic ac magnetic field at the center (see animation in Video S1). (c) Theoretical calculation of two systems with the same majority mobility (μ_p) but different minority mobility (μ_N) under increasing illumination, which yield different conductivity-Hall coefficient (σ - H) curves. The slope of σ - H curve contains the information of $\Delta\mu_H$.

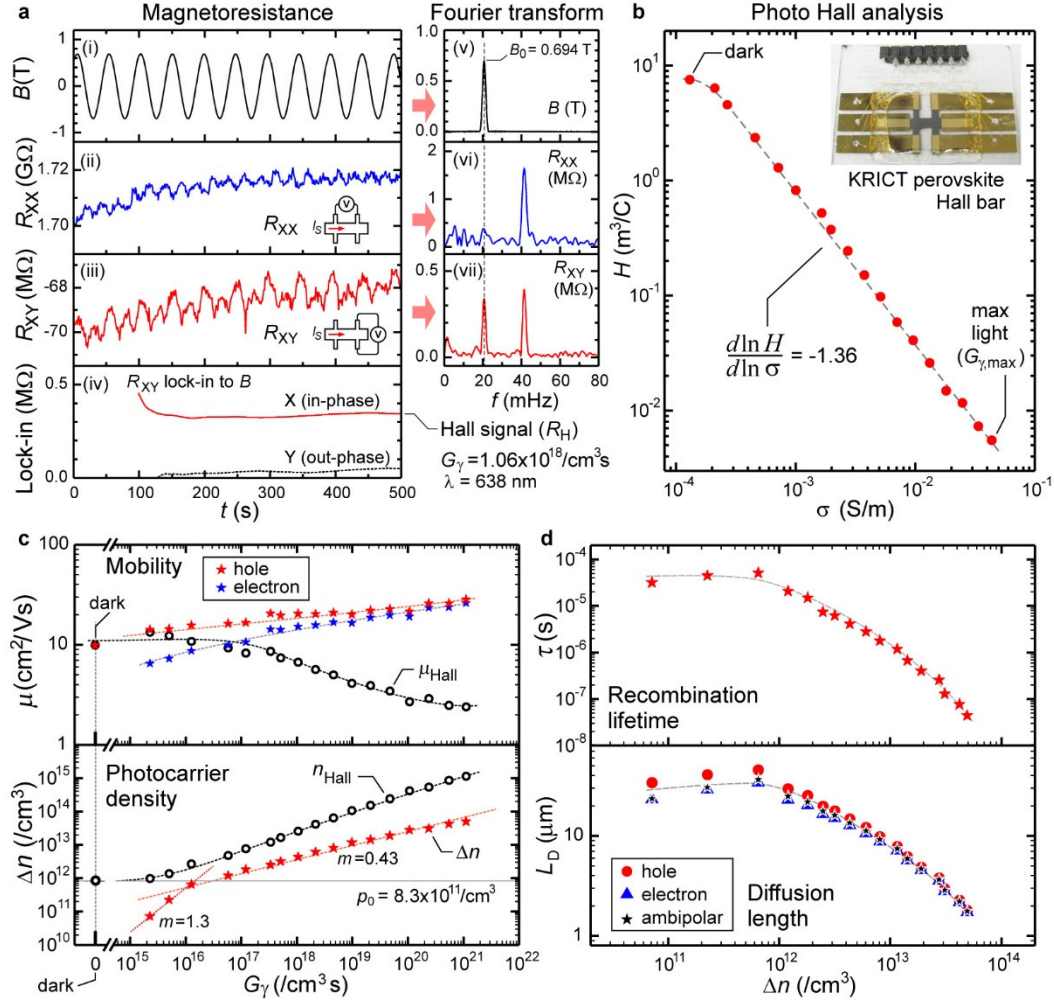


Figure 2. Carrier-resolved photo-Hall analysis in a high-performance perovskite film:
 (a) Magnetoresistance sweep (R_{XX} : longitudinal and R_{XY} : transverse), Fourier transform and lock in detection of the Hall signal (R_{XY}). (b) σ - H plot for photo-Hall analysis. Inset: the perovskite Hall bar device. (c) Results: Majority (μ_P) and minority (μ_N) carrier mobility and photocarrier density Δn vs. absorbed photon density G_γ , with n_{Hall} and μ_{Hall} denoting the "single-carrier" Hall density and mobility. The background carrier density p_0 is indicated using a grey line. (d) Recombination lifetime and diffusion length mapped against Δn . (All dashed curves are guides for the eye only).

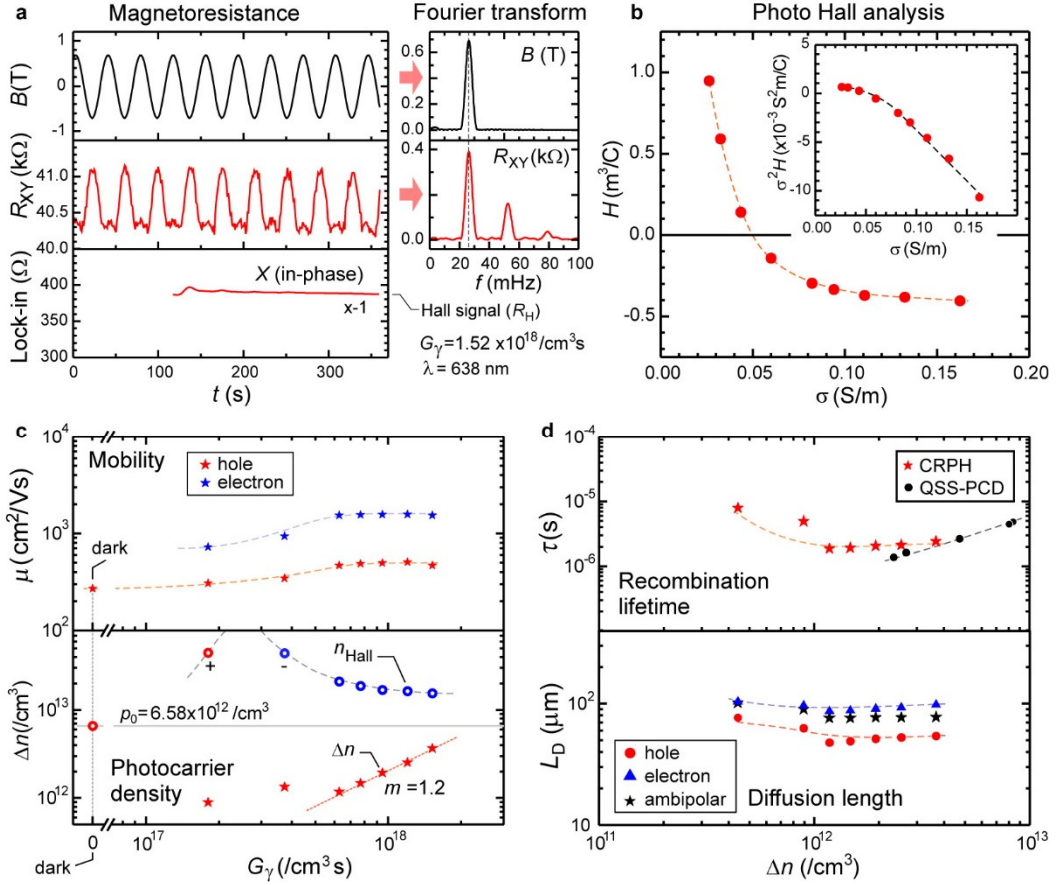
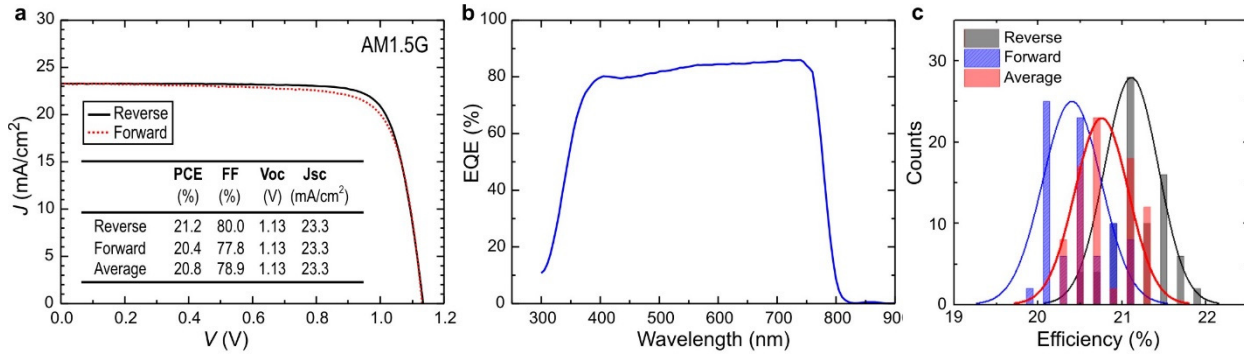
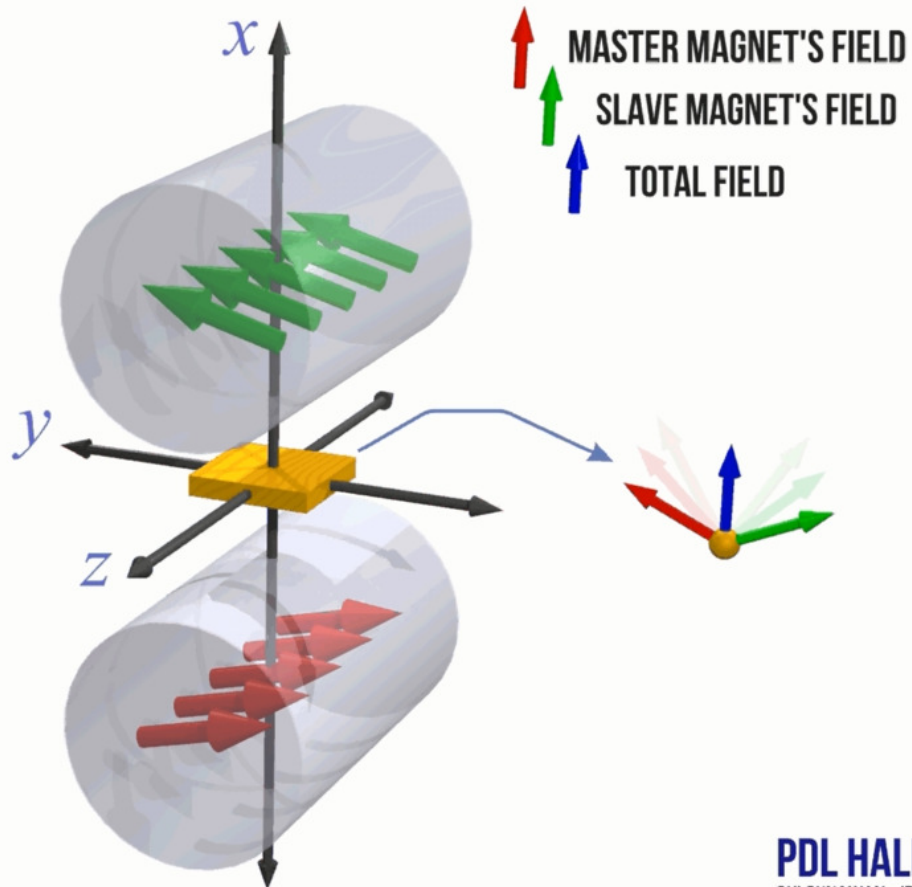


Figure 3. Carrier-resolved photo-Hall analysis in a single crystal P-silicon sample: (a) Transverse magnetoresistance sweep (R_{XY}), Fourier transform and lock-in detection of the Hall signal. (b) σ - H plot for photo-Hall analysis. Inset: Equivalent plot in form of $\sigma^2 H$ vs. σ . (c) Results: Majority (μ_P) and minority (μ_N) mobility and photocarrier density Δn vs. absorbed photon density G_γ , n_{Hall} is the "single-carrier" Hall density. (d) Recombination lifetime and minority carrier diffusion length mapped against Δn . Independent lifetime measurement using quasi-steady-state photoconductance decay (QSS-PCD) technique is shown as black circles. (All dashed curves are guides for the eye only).

Extended Data Figure Legend:



Extended Data Figure 1. Device performance of the $(\text{FAPbI}_3)_{0.88}(\text{MAPbBr}_3)_{0.12}$ solar cell:
 (a) Current density-voltage (J - V) curves measured by reverse and forward scans. The photovoltaic performance values are summarized in the inset. (b) The external quantum efficiency spectrum. (c) Histogram of the power conversion efficiencies obtained from J - V curves measured by reverse scan, forward scan, and average for 80 cells.



PDL HALL SYSTEM
OKI GUNAWAN - IBM RESEARCH (2019)

Video S1. Animation of the rotating parallel dipole line (PDL) Hall system and its field evolution. The master magnet generates a counterclockwise field rotation (red) while the slave magnet follows synchronously but in the opposite direction, generating a clockwise field rotation (green). This results in a total field (blue) that is *unidirectional* (always pointing normal to the sample) and *single harmonic* at the center where the sample resides.

Supplementary Information for:

Carrier-Resolved Photo-Hall Effect

Oki Gunawan^{1*}, Seong Ryul Pae², Douglas M. Bishop¹, Yun Seog Lee^{1,3}, Yudistira Virgus¹, Nam Joong Jeon⁴, Jun Hong Noh^{4,5}, Xiaoyan Shao¹, Teodor Todorov¹, David B. Mitzi^{6,7}, Byungha Shin^{2*}

¹*IBM T. J. Watson Research Center, P.O. Box 218, Yorktown Heights, NY 10598, USA.*

²*Dept. Materials Science and Engineering, Korea Advanced Institute of Science and Technology, 291 Daehak-Ro, Yuseong-Gu, Daejeon 34141, Republic of Korea.*

³*Dept. Mechanical and Aerospace Engineering, Seoul National University, 1 Gwanak-Ro, Gwanak-Gu, Seoul 08826, Republic of Korea.*

⁴*Div. of Advanced Materials, Korea Research Institute of Chemical Technology, 141 Gajeong-ro, Yuseong-Gu, Daejeon 305-600, Republic of Korea.*

⁵*School of Civil, Environmental and Architectural Engineering and Green School, Korea University, Seoul 02841, Republic of Korea.*

⁶*Dept. of Mechanical Engineering and Material Science, Duke University, Durham, NC 27708, USA.*

⁷*Dept. of Chemistry, Duke University, Durham, NC 27708, USA.*

*Corresponding authors: Oki Gunawan:ogunawa@us.ibm.com, Byungha Shin: byungha@kaist.ac.kr

This file includes:

Supplementary Text, section A-H

Figures S1 to S8

Tables S1 to S4

Equations 4 to 38

References 31 to 83

Contents:

A.	The Parallel Dipole Line Hall System	2
B.	The Photo-Hall Equation and Related Formulas	4
C.	Optical Property Determination	10
D.	Time-resolved Photoluminescence Measurement of Perovskite	13
E.	Additional Carrier-Resolved Photo-Hall Studies	14
F.	Summary of Recent Perovskite Transport Studies	17
G.	Summary of Recent Kesterite Transport Studies	19
H.	Device Fabrication and Characteristics of Kesterite	20

A. The Parallel Dipole Line Hall System

Employing an ac magnetic field system is critical for Hall measurement of materials with low mobilities ($\mu < 10 \text{ cm}^2/\text{Vs}$) or high resistivity. Implementation of an ac field with traditional electromagnets is challenging due to highly inductive load impedance that attenuates the output field, which in turn requires a power factor correction technique using a variable capacitor bank system or a special power supply, both of which are costly and inefficient. Commercial ac Hall electromagnet systems are available, but very expensive (>US\$100k); thus, ac field generation systems using permanent magnets have been pursued by many groups^{18,21,22,31,32}.

The parallel dipole line (PDL) Hall system was originally developed to support kesterite $\text{Cu}_2\text{ZnSn}(\text{S},\text{Se})_4$ (CZTSSe) solar cell development at IBM Research¹⁸ and possesses characteristics suitable for high sensitivity ac-Hall and photo-Hall experiments. The system offers few advantages such as: (1) strong magnetic field up to $\sim 2 \text{ T}$ peak-to-peak for PDL gap of 4 mm, (2) pure harmonic and unidirectional ac field generation, (3) compact and low cost setup, and more importantly: (4) ample space that allows directing large area illumination ($\sim 10 \text{ mm} \times 10 \text{ mm}$) to the sample from the side of the PDL magnets (see Fig. 1a). The PDL system is based on a recently-discovered natural magnetic trap that harbors a new type of field confinement effect that forms a camelback field profile along its central longitudinal axis^{18,23}. The PDL Hall system consists of a pair of dipole line or diametric magnets, i.e. cylindrical magnets with uniform transverse magnetization. The diametric magnet produces an exterior magnetic field equal to that of a linear distribution of transverse dipoles¹⁸. This effect is analogous to the fact that a uniformly magnetized sphere produces a perfect point dipole field at its exterior.

To describe the field characteristics of a PDL system, we use the following elegant description suggested by K.T. McDonald³³ (see also ref. 23, Supplementary Material B). Considering a long dipole line (or a long diametric magnet) system, the field distribution can be described by a simple complex potential function of the form $f(u) \sim 1/u$, specifically:

$$f(u) = \frac{M R^2}{2u} , \quad (4)$$

where $u = x + iy$ is a complex number within the x, y coordinate system, M is the volume magnetization of the magnet and R is the magnet radius. The magnetic field outside the magnet is given as:

$$\mathbf{B}(x, y) = -\mu_0 \nabla \text{Re}[f(u)], \quad (5)$$

which yields: $\mathbf{B}(x, y) = \mu_0 M R^2 / 2(x^2 + y^2)^2 \times [(x^2 - y^2)\hat{x} + 2xy\hat{y}]$, where μ_0 is the magnetic permeability in vacuum. This field distribution is plotted in Fig. S1a. Note that the field lines form parts of *perfect circle*²³.

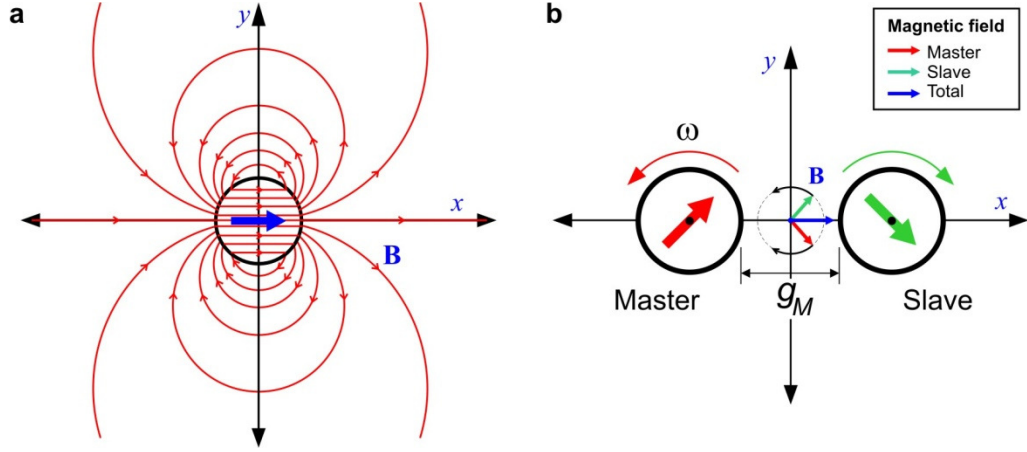


Figure S1. (a) A long dipole line (diametric) magnet and its field distribution. (b) The rotating PDL Hall system and its field evolution (see also Video S1).

In the rotating PDL Hall configuration, we have a pair of diametric magnets whose centers are placed at $(\pm a, 0)$, separated by a gap g_M as shown in Fig. S1b, where $a = R + g_M/2$. The sample is placed at the center, with the sample normal pointing along the x -axis. Only one of the magnets (the "Master") needs to be driven by a motor and gearbox system, with angular speed ω , and the other magnet (the "Slave") synchronously follows in the opposite direction. The complex potential function of such a rotating PDL system is given as:

$$f_T(u) = \frac{MR^2}{2} \left(\frac{e^{i\omega t}}{u-a} + \frac{e^{-i\omega t}}{u+a} \right). \quad (6)$$

The total magnetic field at the center $(0, 0)$ where the sample resides reduces to a very simple form:

$$\mathbf{B}_T(0,0) = -\mu_0 \nabla \operatorname{Re}[f_T(u)] = B_0 \cos \omega t \hat{\mathbf{x}}, \quad \text{with: } B_0 = \frac{\mu_0 M R^2}{(R + g_M/2)^2}. \quad (7)$$

Note that the y -component field vanishes, leaving only the x -component, and a pure single harmonic field term, $\cos \omega t$. The geometric description of the system also provides a simple explanation of this rotating PDL field characteristic, as shown in Fig. S1b. Each magnet produces a counter-rotating field that cancels off the y -component, leaving behind only a total oscillating field in the x -direction. An animation of the PDL field evolution is shown in Video S1, which provides clear visualization of this effect. *We emphasize that this natural field characteristic of the rotating PDL system produces the desired qualities for our photo-Hall experiment: a unidirectional field that mainly excites the desired Hall effect, without any out-of-plane field that may produce an extra parasitic magnetoresistance signal, and a pure harmonic ac field that simplifies the Fourier analysis and lock-in detection.* We also calibrate the magnetic field at the sample position (i.e., placed at the center of the PDL system) for various magnet gaps using a gaussmeter (Lakeshore 410 Gaussmeter). This then represents the amplitude (B_0) of the oscillating field.

Another important design consideration is the size or aspect ratio (length / radius) of the diametric magnet. If the length of the magnet is too short, the field on the sample will be non-uniform, while if it is too long the torque required to drive the system will be unnecessarily large (requiring a more powerful motor or gearbox and causing a more jerky motion due to the large oscillating torque). For this problem we have to recognize the *camelback effect*, which is the central feature of the PDL system that enables it to become a natural diamagnetic trap¹⁸, as shown in Figure S2a. This effect occurs when the length of the dipole line system exceeds a certain critical length L_c , that results in a slightly enhanced field at the edges, thus producing a camelback field profile. Figure S2b also shows the field distribution at the center of the PDL system with different magnet aspect ratios of $L/R = 1, 2$ and 4 . The magnetic field along the z -axis is most uniform when the field profile at the center is flat ($d^2B/dz^2 = 0$). Therefore, we design our PDL magnet length *at the critical length for the camelback effect, which occurs at $L_c \sim 2.5a$, where $2a$ is the separation of the two dipole line system*²³. In the actual setup, when we take into account a typical gap of $g_M \sim 5$ mm, we choose $L \sim 2R$.

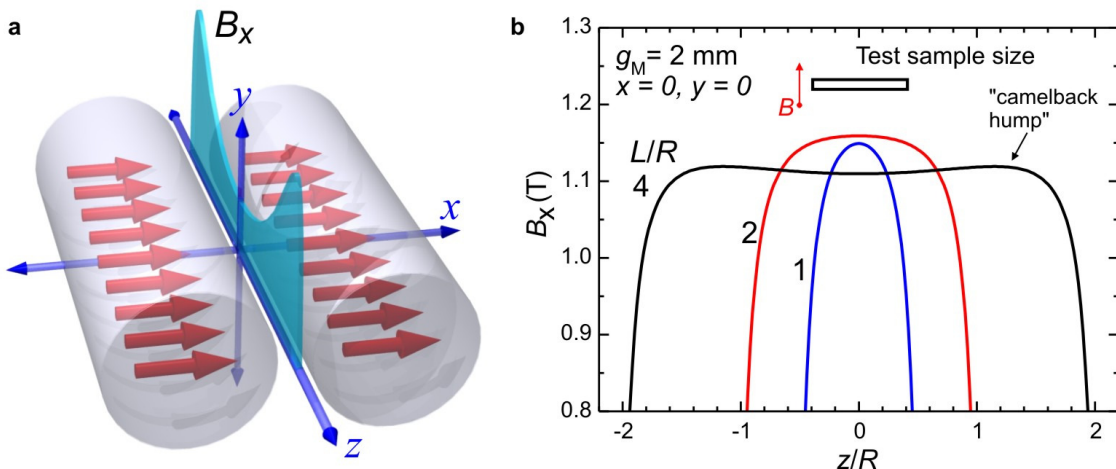


Figure S2. (a) The "camelback effect"²³ in a parallel dipole line system where the magnetic field (B_x) is enhanced at the edges. This effect is used to optimize the field uniformity in the PDL Hall system. (b) The field distribution along the longitudinal axis at various magnet aspect ratios: $L/R = 1, 2$ and 4 .

B. The Photo-Hall Equation and Related Formulas

B.1 Basic $\Delta\mu$ Model (Constant Mobility)

Here we derive the new photo-Hall equation starting from the well-known two-carrier Hall equations in the low field regime ($B \ll 1/\mu$)^{20,34}:

$$\sigma = e(p\mu_p + n\mu_N) \quad (8)$$

$$H = \frac{r(p - \beta^2 n)}{(p + \beta n)^2 e}, \quad (9)$$

where μ_p , μ_N are the hole and electron (drift) mobilities, $\beta = \mu_N / \mu_p$ is the mobility ratio for the electron and hole, and r is the Hall scattering factor that lies between 1 and 2 and becomes closer to 1 at high magnetic field. As the value of r is often unknown, it is frequently assumed to be unity^{19,20}. The Hall scattering factor r relates the drift and Hall mobility as: $\mu_H = r\mu$ (ref. 19, eq. 71). The low field condition is well satisfied in this study, e.g. the maximum mobility for perovskite is of order $10 \text{ cm}^2/\text{Vs}$ and maximum magnetic field used is $\sim 0.7 \text{ T}$; thus, $B \ll 1/\mu$. We use a P -type material as an example, but we emphasize that the photo-Hall identity equation also applies to N -type materials.

In a photo-Hall experiment for a P -type material we have: $p = p_0 + \Delta p$ and $n = \Delta n$. The electron and hole photo-carrier densities, Δn and Δp , respectively, are equal under steady state equilibrium i.e., $\Delta p = \Delta n$. As mentioned in the main text, the key insight in solving the photo-Hall transport problem is to extract the information about the system mobility values from the σ - H curve. The quantities σ and H are actually parametric, as they are obtained experimentally as a function light intensity or absorbed photon density (G_γ). We then have:

$$\sigma = e\mu_p [p_0 + \Delta n(1 + \beta)] \quad (10)$$

$$\frac{d\sigma}{d\Delta n} = e\mu_p(1 + \beta) \quad (11)$$

We assume that the dark or background carrier density p_0 and mobilities are constant in the vicinity of the (σ, H) measurement point where the derivative is evaluated. We can then deduce (from eq. 9) the two-carrier Hall coefficient:

$$H = \frac{r(p_0 + \Delta n(1 - \beta^2))}{[p_0 + \Delta n(1 + \beta)]^2 e} = \frac{r e \mu_p^2 [p_0 + \Delta n(1 - \beta^2)]}{\sigma^2}, \quad \text{and} \quad (12)$$

$$\frac{d(\sigma^2 H)}{d\Delta n} = r e \mu_p^2 (1 - \beta^2) = \frac{d\sigma}{d\Delta n} \frac{r \mu_p (1 - \beta^2)}{1 + \beta} = \frac{d\sigma}{d\Delta n} r \mu_p (1 - \beta) = \frac{d\sigma}{d\Delta n} r \Delta \mu, \quad (13)$$

where $\Delta \mu = \mu_p - \mu_N$ is the (drift) mobility difference. The key insight here is that the dependence on Δn is eliminated; thus, we can relate the mobility difference only to σ and H . For simplicity, we define the "Hall" mobility difference: $\Delta \mu_H = r \Delta \mu$, which can be written as:

$$\Delta \mu_H = \frac{d(\sigma^2 H)}{d\sigma}. \quad (14)$$

This expression suggests that we could extract $\Delta\mu_H$ from the slope of σ^2H vs. σ plot which is an appropriate analysis for photo-Hall measurement in the low-injection regime ($\Delta n < p_0$). We use this approach, for example in analyzing silicon and kesterite samples in this report (see Fig. 3 and Fig. S7). In cases where the mobilities are constant, the σ^2H vs. σ plot is linear and $\Delta\mu_H$ is constant.

Another equivalent form of eq. 14 is given as:

$$\Delta\mu_H = \left(2 + \frac{d \ln H}{d \ln \sigma} \right) \sigma H, \quad (15)$$

This form is more suitable for photo-Hall analysis in high injection regime where $\Delta n > p_0$, such as in perovskite, since the σ - H data is more appropriately presented in the log-log plot. This expression also provides a quick and simple interpretation of the H vs. σ data by looking at the slope in the log-log scale as discussed in the main text, e.g. when the slope $d \ln H / d \ln \sigma = -2$, then both mobility are equal: $\mu_P = \mu_N$. We note that repeating the derivation in eq. 10-13 for an N -type material will lead to the same expressions in eqs. 14 and 15.

Once we know $\Delta\mu$, then we can solve for the photo-Hall transport parameters (β , μ_P , μ_N and Δn) by solving eq. (8) and (9). These solutions are given in Table S1, eq. (16) and (17) (also shown as eq. 2 and 3 in the main text) for P -type and N -type material, respectively. We refer to this solution set as the " $\Delta\mu$ " model. Note that one needs to know the dark or background carrier density, i.e. p_0 for P -type material or n_0 for N -type material, which is obtained from the classic Hall measurement in the dark. In the photo-Hall analysis, it is useful to monitor the "single carrier" Hall mobility: i.e. $\mu_H = \sigma H$ and "single-carrier" Hall density: i.e. $n_H = 1/eH$. In the dark, the single carrier mobility μ_H is certainly equal to the majority carrier mobility and at very high light intensity or very high injection level ($\Delta n \gg p_0$), it can be shown that $\mu_H \rightarrow \Delta\mu_H$ (see e.g. Fig. 2c). Similarly in the dark, the "single carrier" Hall density n_H is equal to the majority carrier density and at very high light intensity or very high injection level ($\Delta n \gg p_0$) we have: $n_H \rightarrow \Delta n(1 + \beta)/(1 - \beta)$.

For completeness and verification purposes, we also present additional trivial photo-Hall solution models i.e., solutions if additional information, such as β , one or two mobilities are known. For example, if we assume a known β , majority mobility (μ_M) or both (" μ_{PN} " for μ_P and μ_N), we can solve the transport problem accordingly. We refer to these as " β ", " μ_M " and " μ_{PN} " models, respectively, as summarized in Table S1 row 2 to 4. These additional models are sometimes useful for checking the overall solutions or when the data are very noisy. In all models, one needs to know the dark carrier density or conductivity (p_0 , n_0 or σ_0).

Table S1. The carrier-resolved photo-Hall solution models and formulas for P and N -type materials

NO	MODEL	TYPE	FORMULA	
1.	$\Delta\mu$	P	$\Delta\mu_H = \frac{d(\sigma^2 H)}{d\sigma}$	$\beta = \frac{2\sigma(r\Delta\mu - \sigma H) - re\Delta\mu^2 p_0 \pm \Delta\mu\sqrt{re p_0} \sqrt{re\Delta\mu^2 p_0 + 4\sigma(\sigma H - r\Delta\mu)}}{2\sigma(r\Delta\mu - \sigma H)}$ $\Delta n = \frac{\sigma(1-\beta) - e\Delta\mu p_0}{e\Delta\mu(1+\beta)}$ (16)
		N	$\mu_p = \frac{\Delta\mu}{1-\beta}$ $\mu_N = \beta\mu_p$	$\beta = \frac{2\sigma(r\Delta\mu - \sigma H) + re\Delta\mu^2 n_0 \pm \Delta\mu\sqrt{re n_0} \sqrt{r\Delta\mu^2 e n_0 + 4\sigma(r\Delta\mu - \sigma H)}}{2\sigma(r\Delta\mu - \sigma H)}$ $\Delta p = \frac{\sigma(1-\beta) - e\Delta\mu n_0 \beta}{e\Delta\mu(1+\beta)}$ (17)
2.	β	P		$\Delta n = \frac{r - 2e p_0 H - r\beta \pm \sqrt{r^2 + r\beta(r\beta + 4e p_0 H - 2r)}}{2e H(1+\beta)}$ $\mu_p = \frac{\sigma}{e[p_0 + \Delta n(1+\beta)]}$ (18)
		N		$\Delta p = \frac{r - 2e n_0 H \beta(1+\beta) - r\beta^2 \pm \sqrt{r(1+\beta)^2(r + \beta[r\beta - 4e n_0 H - 2r])}}{2e H(1+\beta)^2}$ $\mu_N = \frac{\sigma}{e[n_0 + \Delta p(1+\beta)/\beta]}$ (19)
3.	μ_M	P	$\beta = \frac{\sigma}{r\mu_p} \frac{(r\mu_p - \sigma H)}{(\sigma - e p_0 \mu_p)}$	$\Delta n = \frac{\sigma - e\mu_p p_0}{e(1+\beta)\mu_p}$ (20)
		N	$\beta = \frac{\mu_N}{\sigma} \frac{r(\sigma - e n_0 \mu_N)}{(r\mu_N + \sigma H)}$	$\Delta p = \frac{(\sigma - e n_0 \mu_N)\beta}{e\mu_N(1+\beta)}$ (21)
4.	μ_{P-N}	P/N		$\Delta n = \frac{\sigma - \sigma_0}{e(\mu_p + \mu_N)}$ (22)

B.2 Generalized $\Delta\mu$ Model (Varying Mobility)

We describe a generalized photo-Hall identity equation that accounts for varying mobilities. It modifies the basic $\Delta\mu$ model in the previous section that assumes constant mobilities. This model introduces corrections for the perovskite CRPH analysis, especially at high light intensity, where there is an apparent increase in mobility. Mobility could change with increasing light intensity, for

example, due to the filling of the electronic traps or defects and increased screening at higher carrier density.

When the mobilities vary, the photo-Hall identity equation $\Delta\mu_H$ will have additional corrections, which we refer to as the "generalized $\Delta\mu$ model" given as:

$$\Delta\mu_H' = [\Delta\mu_H + c_1]c_2, \quad (23)$$

where the terms c_1 and c_2 (derived in next section) are given as (for *P*-type materials):

$$c_1 = 2e\mu_p \left(\mu_p \Delta n \beta \frac{d\beta}{d\sigma} - e \frac{d\mu_p}{d\sigma} [p_0 + \Delta n(1 - \beta^2)] \right) \quad (24)$$

$$c_2 = \left(1 - e \mu_p \Delta n \frac{d\beta}{d\sigma} - e \frac{d\mu_p}{d\sigma} [p_0 + \Delta n(1 + \beta)] \right)^{-1}. \quad (25)$$

For *N*-type materials, we have:

$$c_1 = 2e\mu_p \left(\mu_p \Delta n \beta \frac{d\beta}{d\sigma} + \mu_p n_0 \beta \frac{d\beta}{d\sigma} - e \frac{d\mu_p}{d\sigma} [\Delta n(1 - \beta^2) - n_0 \beta^2] \right) \quad (26)$$

$$c_2 = \left(1 - e \mu_p \left(\Delta n \frac{d\beta}{d\sigma} + n_0 \frac{d\beta}{d\sigma} \right) - e \frac{d\mu_p}{d\sigma} [\Delta n(1 + \beta) + n_0 \beta] \right)^{-1}. \quad (27)$$

The new term c_1 and c_2 reflect the offset and scaling factor modifications of $\Delta\mu_H$. Note that when the mobilities (μ_p and μ_N) are constant we have $c_1 = 0$ and $c_2 = 1$ and eq. 23 reduces to eq. 1. In this generalized model, we still use eqs. 2 and 3 to calculate the mobility ratio β and Δn .

In practice, the evaluation of c_1 and c_2 requires the knowledge of μ_p and μ_N (or β) vs. σ , which are initially unknown. Thus, an iterative process is needed for a self-consistent solution. First, we attempt the baseline solution assuming a constant mobility using eqs. 1-3. If the results produce reasonably constant mobilities, we accept this as the final solution; however, if the results show varying mobilities, we then calculate the constants c_1 and c_2 and the new $\Delta\mu$ using eq. 23. We then proceed to calculate μ_p , μ_N , and Δn again using eqs. 2 and 3 until we arrive at converged solutions, for which the $\Delta\mu$ remains practically constant after several iterations (and thus μ_p , μ_N , and Δn).

B.3 Derivation of the Generalized $\Delta\mu$ Model:

We obtain the generalized $\Delta\mu$ equation (eq. 23) by repeating the derivation of the basic $\Delta\mu$ equation in Section B.1, but by considering varying mobilities: $d\mu_p/d\sigma \neq 0$ and $d\beta/d\sigma \neq 0$. We use a *P*-type material as an example. For the conductivity we have:

$$\frac{d\sigma}{d\Delta n} = e\mu_p(1+\beta) + e\mu_p\Delta n \frac{d\beta}{d\Delta n} + e \frac{d\mu_p}{d\Delta n} [p_0 + \Delta n(1+\beta)] \quad (28)$$

$$e\mu_p(1+\beta) = \frac{d\sigma}{d\Delta n} - e\mu_p\Delta n \frac{d\beta}{d\Delta n} - e \frac{d\mu_p}{d\Delta n} [p_0 + \Delta n(1+\beta)] \quad (29)$$

We combine both σ and H and find their derivatives:

$$\frac{d(\sigma^2 H)}{rd\Delta n} = e\mu_p^2(1-\beta^2) - 2e\mu_p^2\Delta n\beta \frac{d\beta}{d\Delta n} + 2e\mu_p \frac{d\mu_p}{d\Delta n} [p_0 + \Delta n(1-\beta^2)] \quad (30)$$

$$e\mu_p^2(1-\beta^2) = \frac{d(\sigma^2 H)}{rd\Delta n} + 2e\mu_p^2\Delta n\beta \frac{d\beta}{d\Delta n} - 2e\mu_p \frac{d\mu_p}{d\Delta n} [p_0 + \Delta n(1-\beta^2)] \quad (31)$$

By dividing eq. (31) and (29), we obtain the generalized equation for $\Delta\mu$ that accounts for varying mobilities:

$$\Delta\mu_H' = \frac{e\mu_p^2(1-\beta^2)}{e\mu_p(1+\beta)} = \left[\frac{d(\sigma^2 H)}{d\sigma} + c_1 \right] c_2 = [\Delta\mu_H + c_1] c_2 \quad (32)$$

Derivation for N -type materials is similar to the steps above, with c_1 and c_2 given in eq. (24) to (27).

B.4 Application of the Generalized $\Delta\mu$ Model:

We apply the generalized $\Delta\mu$ model when we have significant slope in the mobility ($d\mu_p/d\sigma$) or its ratio ($d\beta/d\sigma$), especially in the high light intensity regime (since, for low intensity, the data are generally more noisy). As an example, we can consider the perovskite case. First, we calculate the baseline mobility difference ($\Delta\mu$) using eq. 1, which assumes constant mobility. Then, we proceed to calculate the solutions (μ_P , μ_N and Δn) using eq. 2 and 3. An example of the first iteration of $\Delta\mu$ and μ_P calculation is shown in Figure S3. We notice that there is a significant slope in μ_P as a function of conductivity σ , thus prompting us to proceed to calculate c_1 and c_2 (eqs. 24-27). The numerical derivative operation is generally noisy; thus, we fit the μ_P and β vs. σ data with smoothed curves, from which we can calculate the slopes $d\mu_p/d\sigma$ and $d\beta/d\sigma$ to obtain c_1 and c_2 . We subsequently proceed with the next iteration to obtain the new $\Delta\mu$ value, using the generalized model (eq. 23), and calculate a new set of solutions (μ_P , μ_N and Δn). This iteration is continued until there is practically no more changes in the $\Delta\mu$ vs. σ plot with successive iteration, which indicates that the solution has converged. We track the average changes of $\Delta\mu$ at every iteration (see Figure S4) and observe that there are initially large changes in $\Delta\mu$ (~10%). However, after about 20 iterations, the solutions converge, which indicates that the final solution has been

obtained. This generalized model correction reduces the initial solution for μ_P by $\sim 2\times$ at the highest light intensity.

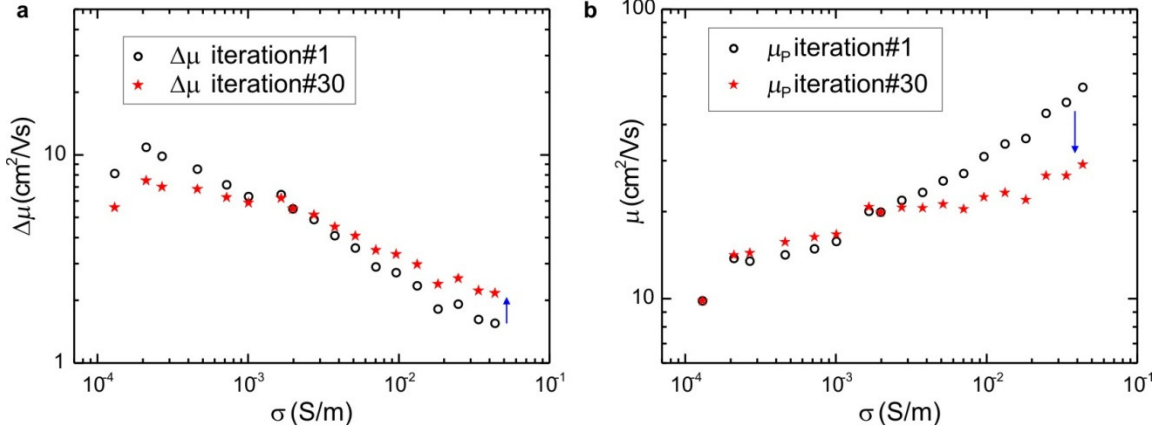


Figure S3. Iterative process for calculating the photo-Hall solutions of the (FA,MA)Pb(I,Br)₃ perovskite sample in Fig. 2: (a) Mobility difference $\Delta\mu$. (b) Hole mobility (μ_P).

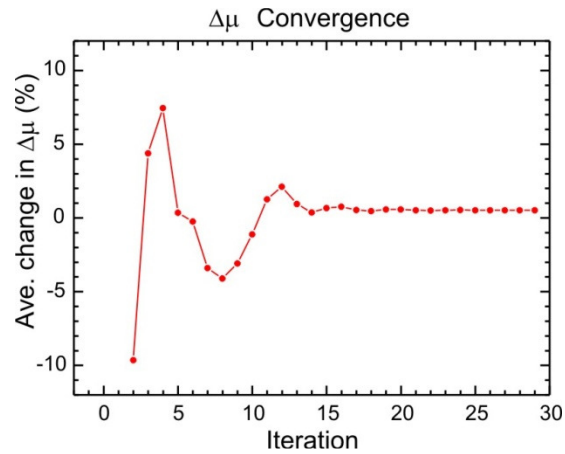


Figure S4. Iteration of the generalized $\Delta\mu$ model calculation showing the average error in $\Delta\mu$ of the i -th iteration. The solution converges after approximately 20 iterations.

C. Optical Property Determination

In this section we describe the determination of the absorbed photon density and the related optical properties of the films. Consider a slab of semiconductor material under illumination. The absorbed photo density rate (G_γ) of a monochromatic illumination at wavelength λ varies exponentially with respect to absorption coefficient (ref. 20, eq. A7.4):

$$G_{\gamma,x}(x, \lambda) = [1 - R(\lambda)] \Phi(\lambda) \alpha(\lambda) \exp(-\alpha(\lambda)x), \quad (33)$$

where R is the reflectivity, α is the absorption coefficient, Φ is the impinging photon flux and x is the depth from the illuminated surface. Using this equation and a steady state diffusion equation, one can calculate the excess carrier density profile in the sample $\Delta n(x)$ (cf. ref. 20, appendix 7.1).

We can then calculate the average G_γ in the sample of thickness d :

$$G_\gamma = \int_0^d G_{\gamma,x}(x) dx / d = (1 - R) \Phi [1 - \exp(-\alpha d)] / d. \quad (34)$$

Note that, for an optically thin sample ($d \ll 1/\alpha$), we have $G_\gamma = (1 - R) \Phi \alpha$. The photocarrier generation rate is given as $G = \eta G_\gamma$ where η is the photocarrier generation efficiency, which is often assumed to be unity.

Note that, even though in most cases the absorption depth is smaller compared to the thickness, the actual photocarrier density distribution becomes more uniformly distributed due to the diffusion process, which is more correct for samples with long diffusion lengths. More quantitatively, the distribution of the carrier density in such a sample is given as³⁵:

$$\Delta n(x) = \frac{(1 - R)\Phi \alpha \tau}{(\alpha^2 L_D^2 - 1)} \left[\frac{A_1 + B_1 e^{-\alpha d}}{D_1} - \exp(-\alpha d) \right], \quad (35)$$

where A_1 , B_1 , and D_1 are coefficients that depend on α , L_D and surface recombination coefficients, as described in ref. 20, appendix 7.1.

In the current experiment, we determine the absorbed photon density G_γ in the sample as follows. The impinging photon flux density, Φ , is related to the photocurrent reading from the monitor photodetector (PD) I_{PD-MON} using:

$$\Phi = \frac{I_{PD-MON} k_{PD}}{e Q E_{REF}(\lambda) A_{REF}} , \quad (36)$$

where $Q E_{REF}$ is the quantum efficiency of the Reference PD at wavelength λ , A_{REF} is the effective area of the Reference PD ($A_{REF} = 7.5 \text{ mm}^2$) and k_{PD} is the PD calibration factor measured after the photo-Hall measurement session is completed.

We define an experimental constant k_G that depends on the operating wavelength λ :

$$k_G(\lambda) = \frac{k_{PD} [1 - R(\lambda)]}{e Q E_{REF}(\lambda) A_{REF}} \frac{[1 - \exp(-\alpha(\lambda)d)]}{d}. \quad (37)$$

Thus, employing eqs. 34, 36 and 37, we can calculate G_γ directly from the Monitor PD current (I_{PD-MON}):

$$G_\gamma = k_G(\lambda) I_{PD-MON} . \quad (38)$$

For the G_γ calculation, we need the reflectivity and absorption coefficient data. These values can be measured using the same photo-Hall setup as shown in Fig. 1a, by deflecting the laser beam with a prism. For absorption (or transmission) measurement, the sample-under-test is mounted before the "Transmission photodetector (PD)". For reflectivity measurement, we use a silicon photodetector ("Reflectivity PD") embedded inside an integrating sphere (diameter ~80 mm). The sample is placed under an integrating sphere on a wedge to partially deflect the beam into the integrating sphere, where the light is collected by the photodetector. A certified reflectance disc (LabSphere SRS-80-010) is used as reference or calibration standard. The absorption coefficient at the given wavelength λ can be calculated using these reflectivity and transmission coefficients using the method detailed in ref. 36. Alternatively, one could use the absorption coefficient from standard absorption spectroscopy measurement. Table S2 below summarizes the optical parameters for the samples used in this study:

Table S2. The optical parameters for the perovskite, silicon and kesterite samples in this study

No	Sample	d (μm)	λ (nm)	k_{PD}	QE_{REF}	R	α (/cm)	k_G (/ Acm^3s)
1.	Perovskite (FA,MA)Pb(I,Br) ₃	0.55	638	0.777	0.790	0.481	4.58x10 ⁴	7.1x10 ²³
2.	Perovskite MAPbI ₃	0.608	638	0.874	0.790	0.442	4.90x10 ⁴	8.0x10 ²³
3.	Silicon	725	638	0.813	0.790	0.347	3.09x10 ⁴	7.71x10 ²⁰
4.	Kesterite	2	450	1.17	0.474	0.286	4.88x10 ⁴	7.35x10 ²³

D. Time-Resolved Photoluminescence Measurement of Perovskite

In Fig. 2c, the Δn vs. G_γ data show a regime with $m \sim 0.5$ for $\Delta n \sim G_\gamma^m$, which could be ascribed to operating within the bimolecular recombination regime. To investigate the possibility of (band-to-band) bimolecular recombination, we attempted to measure the bimolecular recombination coefficient k_2 , where $G = k_2 \Delta n^2$, using time-resolved photoluminescence (TRPL). The TRPL measurements are performed on a (FA,MA)Pb(I,Br)₃ perovskite film of the same composition as

used for the CRPH experiment. The measurement was performed using a Hamamatsu TR-PL system with laser wavelength $\lambda=532$ nm and pulse rate 15 kHz at room temperature. At maximum intensity of ~ 4 W/cm² we estimate the initial carrier injection level of $\Delta n_0 \sim 7 \times 10^{19}/\text{cm}^3$. Several TRPL curves at different initial injection (or laser fluence) levels are shown in Fig. S5a. At the lowest fluence where the PL signal still can be observed, we estimate that the initial carrier density generated is $\Delta n_0 \sim 10^{18}/\text{cm}^3$. The curves are fitted following a procedure similar to that described in ref. 37 using the rate decay equation up to 3rd order: $PL(t) \propto \Delta n(t)$ and $d\Delta n(t)/dt = -k_1\Delta n(t) - k_2\Delta n(t)^2 - k_3\Delta n(t)^3$, where $PL(t)$ is the photoluminescence signal, k_1 , k_2 and k_3 are the monomolecular, bimolecular and Auger recombination coefficients, respectively. Then, we extract the coefficients k_1 and k_2 .

The above analysis yields a very small ($k_3 \ll 10^{-30}$ cm⁶/s) Auger term k_3 and thus it can be neglected. Our k_2 values of $(0.4-1.5) \times 10^{-10}$ cm³/s from TRPL, as shown in Fig. S5b, are consistent with various other measurements using TR-PL, TAS or THz that report $k_2 = 10^{-11}-10^{-9}$ cm³/s (see Table S3). For this k_2 range and given the expected photo density of $\Delta n \sim 10^{17}-10^{18}/\text{cm}^3$ in the bimolecular regime^{26,28}, we need $G_\gamma = 10^{24}/\text{cm}^3\text{s}$, which is 1000 \times beyond the maximum light intensity in our CRPH experiment ($G_\gamma = 10^{21}/\text{cm}^3\text{s}$). Therefore, the $m \sim 0.5$ behavior in our perovskite Δn vs. G_γ data is not due to band-to-band bimolecular recombination, but rather to a trapping effect as explained in the main text.

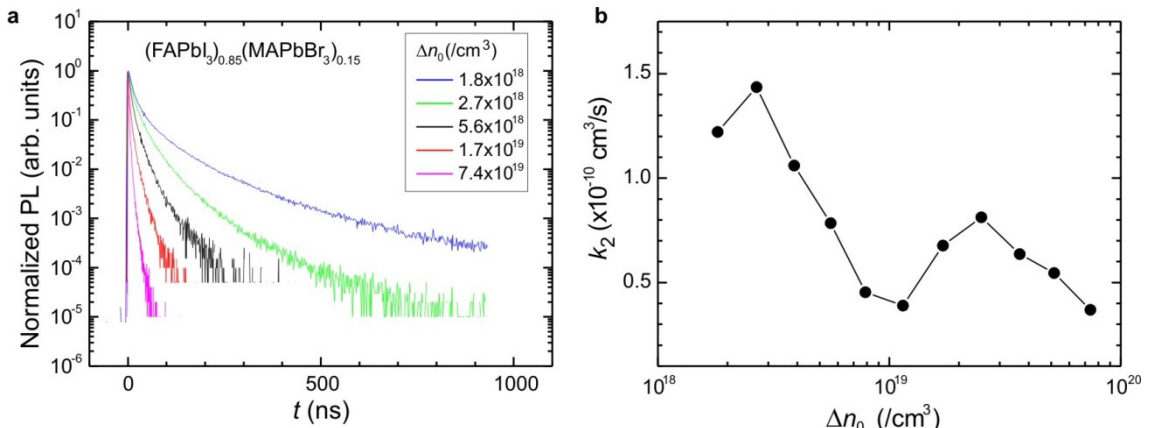


Figure S5. (a) The TR-PL of the (FA,MA)Pb(I,Br)₃perovskite sample at various intensity or carrier injection level Δn_0 . (b) The bimolecular recombination coefficient k_2 vs. initial injection level (Δn_0).

E. Additional Carrier-Resolved Photo-Hall Studies

We present additional Carrier-Resolved Photo-Hall studies in a MAPbI_3 perovskite and a kesterite sample. The related optical properties of the samples are also shown in Table S2.

E.1 Perovskite MAPbI_3

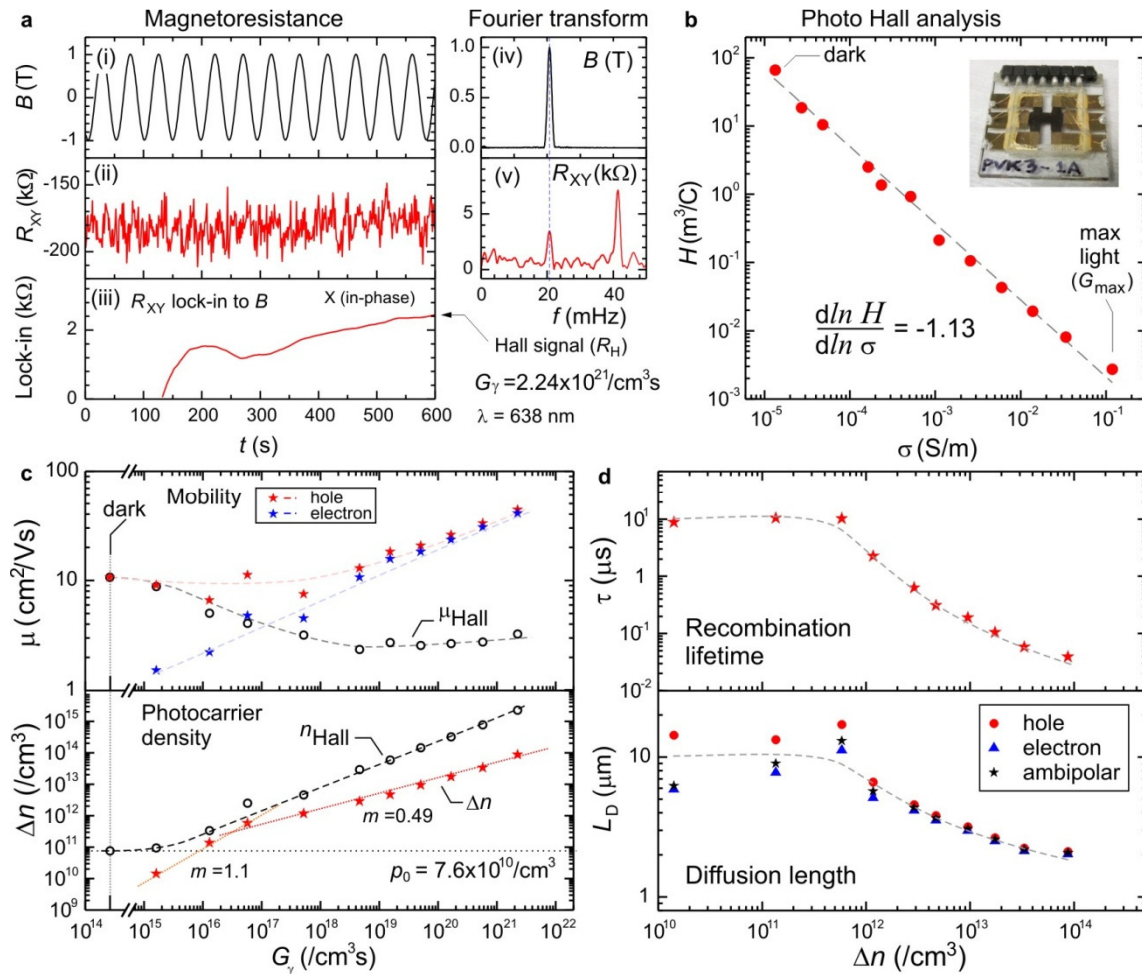


Figure S6. Carrier-resolved photo-Hall analysis in a MAPbI_3 perovskite: (a) Transverse magnetoresistance sweep (R_{XY}), Fourier transform and lock-in detection of the Hall signal. (b) σ - H plot for photo-Hall analysis. Inset: the perovskite Hall bar device. (c) Results: Majority (μ_p) and minority (μ_n) mobility and photo-carrier density Δn vs. absorbed photon density G_γ ; n_{Hall} and μ_{Hall} are the "single-carrier" Hall density and mobility. (d) Recombination lifetime and diffusion length mapped against Δn (all dashed curves are guides for the eye only).

We have also prepared a MAPbI_3 perovskite Hall bar sample as shown in the inset Fig. S6b (thickness $d = 0.608 \mu\text{m}$, active area $W \times L = 2 \text{ mm} \times 4 \text{ mm}$). The results of the CRPH study are shown in Fig. S6. Similar to the $(\text{FA,MA})\text{Pb}(\text{I},\text{Br})_3$ perovskite study in the main text (Fig. 2), we

also found increasing mobilities with respect to light intensity. Therefore we also employed the generalized $\Delta\mu$ model and its iterative solution approach to obtain the final solutions, as described in SI section B.2. We obtain the following results: $\mu_P = 10\text{-}40 \text{ cm}^2/\text{Vs}$, $\mu_N = 2\text{-}40 \text{ cm}^2/\text{Vs}$, $\tau = 40 \text{ ns}$ – $10 \mu\text{s}$, ambipolar $L_D = 2\text{-}10 \mu\text{m}$. These parameters are comparable to the results from the perovskite (FA,MA)Pb(I,Br)₃ in Fig. 2; however, the MAPbI₃ sample seems to have larger recombination coefficient: $k_1 = (1.0 \pm 0.1) \times 10^5 \text{ /s}$. These results are also summarized in Table S3 (last row).

E.2 Kesterite Cu₂ZnSn(S,Se)₄

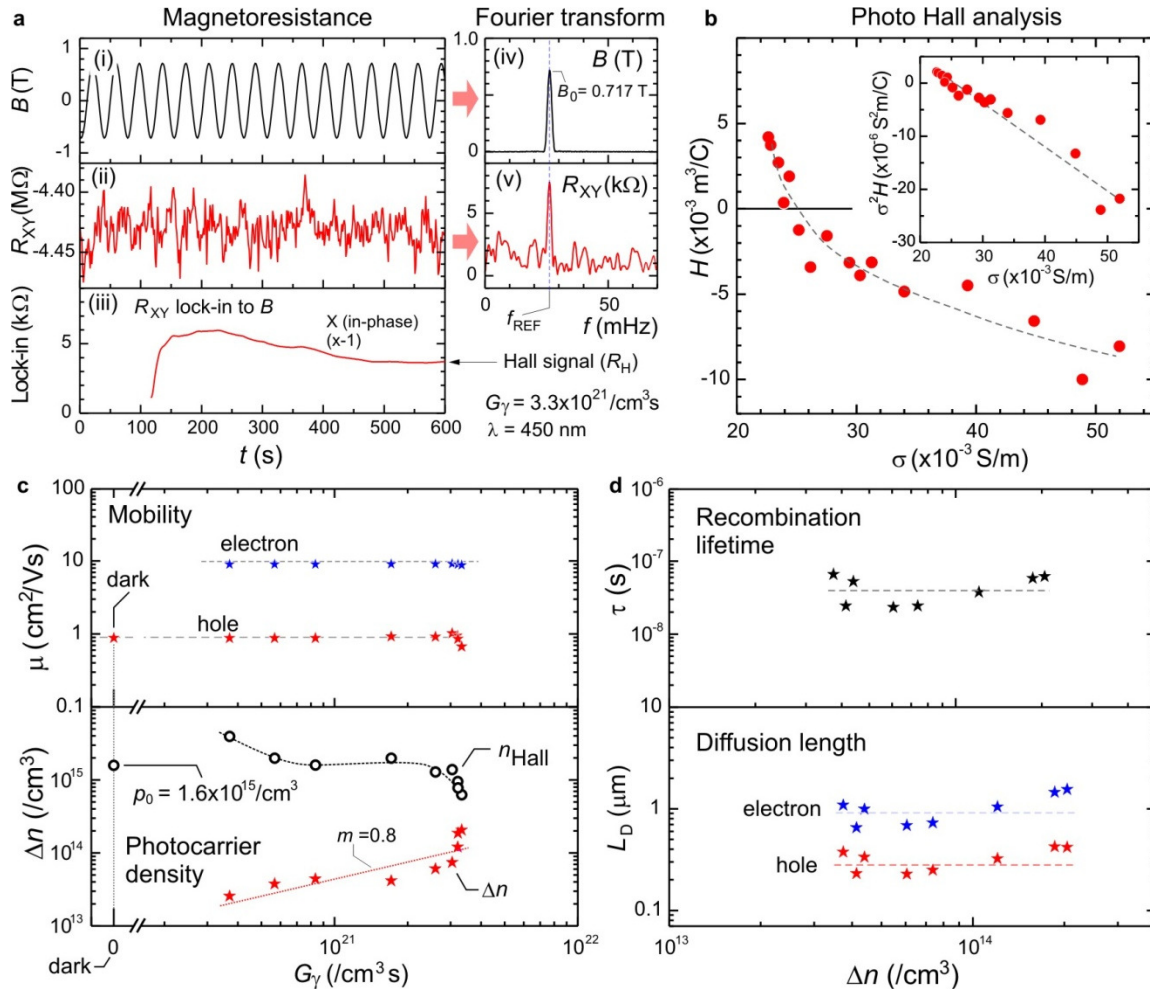


Figure S7. Carrier-resolved photo-Hall analysis in a high performance kesterite film: (a) Magnetoresistance sweep, Fourier transform and lock-in detection of the Hall signal. (b) σ - H plot for photo-Hall analysis showing inversion of H . Inset: σ - H vs. σ plot. (c) Results: Majority (μ_P) and minority (μ_N) mobility and photo-carrier density Δn vs. absorbed photon density G_γ . (d) Recombination lifetime and diffusion length of both hole and electron mapped against Δn . (All dashed curves are guides for the eye only).

A thin-film semiconductor absorber, kesterite $\text{Cu}_2\text{ZnSn}(\text{S},\text{Se})_4$ (CZTSSe), has also garnered significant interest due to its earth abundant and non-toxic elemental composition, as well as improved thermodynamic stability in comparison to perovskites³⁸. Therefore, we present a study on a high performance CZTSSe film. The sample fabrication and solar cell performance information is provided in Section H. The kesterite sample provides an interesting example of low injection regime ($\Delta n < p_0$), due to the much larger p_0 ($\sim 2000\times$) compared to perovskite. Additionally, due to a significantly higher minority carrier (electron) mobility that dominates the conductivity at high light intensity, the sign of H becomes inverted. We perform the experiment on a CZTSSe van-der Pauw sample ($d = 2 \mu\text{m}$) using a blue laser ($\lambda = 450 \text{ nm}$, with intensity up to $\sim 300 \text{ mW/cm}^2$). In the dark, the sample shows P -type conductivity with $p_0 = 1.6 \times 10^{15} \text{ /cm}^3$ and $\mu_p = 0.9 \text{ cm}^2/\text{Vs}$. At the brightest light intensity, the R_{XY} signal shows a clear and robust Fourier peak at f_{REF} [Fig. S7a(v)], which produces a steady lock-in output R_H . We then plot the σ - H curve in Fig. S7b and observe a monotonic behavior. The H data are rather noisy due to the low majority carrier mobility. To calculate $\Delta\mu$ we use eq. 1, i.e., $\Delta\mu_H = d(\sigma^2 H)/d\sigma$, and plot $\sigma^2 H$ vs. σ (Fig. S7b inset) and obtain its slope. We then solve for Δn , μ_p and μ_n using the " $\Delta\mu$ " model as shown in Fig. S7c. We limit our analysis to the high light intensity regime (approximately $\Delta n > p_0/100$), as we cannot resolve Δn when it is too small. We obtain fairly constant mobilities and a significantly higher minority carrier mobility, $\mu_n = (9.0 \pm 0.1) \text{ cm}^2/\text{Vs}$, compared to the majority carrier value, $\mu_p = (0.9 \pm 0.1) \text{ cm}^2/\text{Vs}$ ($\beta \sim 10\times$), which explains the strong H inversion at high light intensity. From Δn vs. G_γ data, we obtain $m = (0.8 \pm 0.2)$, suggesting a monomolecular regime with $k_1 = (3.0 \pm 1.3) \times 10^7 \text{ /s}$. This value is reasonable for the low injection case where $\Delta n < p_0$, and it is also observed in perovskite data at low light intensity (Fig. 2c).

As before, we calculate τ and L_D as a function of Δn (Fig. S7d), obtaining $\tau = (23-66) \text{ ns}$, minority carrier diffusion length $L_{D,N} = (0.7-1.5) \mu\text{m}$ and majority carrier diffusion length $L_{D,P} = (0.23-0.42) \mu\text{m}$. For comparison, our $L_{D,N}$ values overlap and are consistent with independent studies on similar quality samples using: (1) a biased-quantum efficiency technique that yields $L_{D,N} \sim 1.0 \mu\text{m}^{14}$, and (2) an electron-beam-induced-current mapping technique that yields $L_{D,N} \sim (0.75 \pm 0.15) \mu\text{m}^{38}$ (see Table S4). We highlight that the CRPH study was done on a bare absorber layer, which should more accurately reflect the intrinsic properties of the studied semiconductor, because of lack of junction-mediated charge carrier separation, as well as provide a more favorable configuration for higher throughput characterization. This technique also provides simultaneous extraction of all carrier parameters under the same light conditions, which avoids the complication of different light illumination in our previous study¹⁴. The results are compared with various recent transport studies in CZTSSe in Table S4.

We also note that the CRPH analysis data for kesterite is more noisy compared to that for the perovskite and silicon samples for a few reasons: (i) The mobility values in CZTS are small ($\mu_p \sim 1 \text{ cm}^2/\text{Vs}$ and $\mu_n \sim 10 \text{ cm}^2/\text{Vs}$), while in perovskite we have $\mu \sim 10-30 \text{ cm}^2/\text{Vs}$ and for silicon $\mu \sim 500-1500 \text{ cm}^2/\text{Vs}$. (ii) Background carrier density in the CZTS sample is very high ($p_0 \sim 10^{15} \text{ /cm}^3$) compared to the perovskite ($p_0 \sim 8 \times 10^{11} \text{ /cm}^3$) and silicon: ($p_0 \sim 7 \times 10^{12} \text{ /cm}^3$) samples. Since the maximum laser intensity is limited, we could only achieve a maximum photocarrier density of $\Delta n \sim 10^{14} \text{ /cm}^3$, which is $\sim 10\%$ of p_0 ; therefore the CZTS sample is in the very low injection level regime ($\Delta n < p_0$). It is more challenging to extract Δn , as it entails measuring the change in conductivity and Hall coefficient very accurately.

F. Summary of Recent Perovskite Transport Studies

Table S3. Summary of recent electrical transport studies for lead(II) halide perovskites. The results from the current carrier-resolved photo-Hall effect study are highlighted in yellow.

No	Refs	Material	Type	Techniques	Lifetime (ns)	Diffusion Length (μm)		Mobility (cm ² /Vs)		Carrier conc. (/cm ³)		k_f (/s)
						Electron	Hole	Electron	Hole	Electron	Hole	
1	[8]	CH ₃ NH ₃ PbI ₃	pc	PL, transient absorption.	4.5±0.3	0.13	0.11					
2	[9]	CH ₃ NH ₃ PbI _{3-x} Cl _x	pc	Transient absorption, PL-quenching.	273±7	1.07±0.20	1.21±0.24					
		CH ₃ NH ₃ PbI ₃			9.6	0.13±0.04	0.11±0.03					
3	[39]	CH ₃ NH ₃ PbI ₃	pc	Intensity-modulated photocurrent/photovoltage.		1.2 - 1.5						
4	[6]	CH ₃ NH ₃ PbI ₃	pc	PL, transient absorption, time-resolved terahertz and microwave conductivity				12.5	7.5			
5	[10]	CH ₃ NH ₃ PbI _{3-x} Cl _x	pc	Ultrafast THz spectroscopy		2.7*		33*				1.2x10 ⁷
6	[7]	CH ₃ NH ₃ PbI _{3-x} Cl _x	pc	Conductivity measurement. Total mobility used (e + h), assuming similar mass				20	20			
7	[40]	CH ₃ NH ₃ PbI ₃	pc	Laser-flash time-resolved microwave conductivity				3	17			
8	[41]	CH ₃ NH ₃ PbI ₃	pc	Hall effect				13.7-36.0		(2.4-5.9)x10 ¹⁴		
9	[31]	CH ₃ NH ₃ PbI ₃	pc	Hall effect				3.9		2.8x10 ¹⁷		
10	[42]	CH ₃ NH ₃ PbI ₃	pc	Transient PL	9							10 ⁵⁻⁹
		CH ₃ NH ₃ PbI _{3-x} Cl _x	pc		80							
11	[43]	CH ₃ NH ₃ PbI ₃	pc	TR-PL, transient absorption	140							1.8x10 ⁷
12	[27]	CH ₃ NH ₃ PbI ₃	pc	Transient THz spectroscopy				~1*		8.1*		
		CH ₃ NH ₃ PbI _{3-x} Cl _x						~1*		11.6*		1.4x10 ⁶
13	[11]	CH ₃ NH ₃ PbI ₃	sc	PL, transient absorption, Hall effect, time-of-flight measurement, space-charge-limited current technique	22-1032	8*		2.5*				2x10 ¹⁰
		CH ₃ NH ₃ PbBr ₃	sc		41-357	17*			20-115			5x10 ⁹⁻¹⁰
14	[12]	CH ₃ NH ₃ PbI ₃	sc	Transient photovoltaic and impedance spectroscopy, Hall effect	82-95		175±25	24±4.1	164±25		(9±2)x10 ⁹	
15	[37]	CH ₃ NH ₃ PbI _{3-x} Cl _x	pc	Confocal fluorescence microscopy, PL	1005							1x10 ⁶
16	[44]	CH ₃ NH ₃ PbBr ₃ (Cl)	pc	Electron-beam-induced current	50-100	0.36±0.02						
17	[45]	FAPbBr ₃	pc	THz transient photoconductivity		1.3*		14±2*				2.1x10 ⁷
		FAPbI ₃	pc			3.1*		27±2*				6.7x10 ⁸
18	[46]	CH ₃ NH ₃ PbI ₃	pc	Time resolved microwave conductivity				29±6*				
19	[47]	FAPbI ₃	sc	Space-charge-limited current		6.6*				35		3.9x10 ⁹
		FAPbBr ₃	sc			19*				62		1.5x10 ⁹
20	[13]	CH ₃ NH ₃ PbI ₃	pc	Photo-Hall, photoconductivity.	3x10 ⁴	23*		8*				9.0x10 ¹⁴
		CH ₃ NH ₃ PbBr ₃			3x10 ⁶	650*		60±5*				4.6x10 ¹²
21	[48]	CH ₃ NH ₃ PbI ₃	sc	TR-PL, time-resolved microwave conductance	15,000	8	50					
22	[49]	CH ₃ NH ₃ PbI ₃	pc	Transient photovoltage, charge carrier extraction under 1 sun. (Carrier density under illumination)	390							9.4x10 ¹⁸
		CH ₃ NH ₃ PbX ₃			560 -1100							(2.4-5.9)x10 ¹⁹
23	[50]	CH ₃ NH ₃ PbI ₃	pc	Hall and magnetoresistance. (Mobility values under illumination)	29,000	230*		68*				9.3x10 ¹¹
		CH ₃ NH ₃ PbBr ₃	pc		36,000	24*		6.3*				4.3x10 ¹²
24	[51]	FAPbI _{3-x} Cl _x	pc	Flash-photolysis time-resolved microwave conductivity. **Sum of mobility	2,800			71**				
25	[51]	(FAPbI _{3-x} Cl _x) (MAPbBr ₃) _x	pc	Carrier-resolved photo-Hall effect Values are mapped against G_γ or Δn (Fig. 2) (IBM/KAIST/KRICT)	44-40,000	1.7-23	1.8-34	7-26	10-28	8.3x10 ¹¹	2.5x10 ⁴	$\tau(G_\gamma)$
						$L_{D,N}(G_\gamma)$	$L_{D,P}(G_\gamma)$	$\mu_n(G_\gamma)$	$\mu_p(G_\gamma)$	$\Delta n(G_\gamma)$	$p_0 + \Delta n(G_\gamma)$	
26		MAPbI ₃	pc	Carrier-resolved photo-Hall effect Values are mapped against G_γ or Δn (Fig. 2) (IBM/KAIST/KRICT)	40-10,000	2-8	1.8-12	2-40	10-44	7.6x10 ¹⁰	1.0x10 ⁵	$\tau(G_\gamma)$
						$L_{D,N}(G_\gamma)$	$L_{D,P}(G_\gamma)$	$\mu_n(G_\gamma)$	$\mu_p(G_\gamma)$	$\Delta n(G_\gamma)$	$p_0 + \Delta n(G_\gamma)$	

Notes: (1) *Carrier type is not specified (not-resolved). (2) pc = poly crystalline, sc = single crystal

From Table S3 above, we observe that there is a wide range of variation of the transport parameters, with some overlap with our CRPH results. The variation in parameter values most likely arises due to sample variation in terms of quality and passivation, stoichiometry, crystallinity type (poly or single crystal) and varying device performance levels. A second reason is likely the different measurement techniques employed. We note that our CRPH technique operates under (1) steady-state and (2) large illumination coverage (3) with light intensity up to ~1 sun (100 mW/cm²), which is very close to the actual condition where the solar cell is intended to operate. In contrast, most of the other transient techniques, such as time-resolved photoluminescence (TR-PL), do not operate under these conditions, which may lead to variation in the extracted parameters compared to the CRPH results. Below are some comments on the variation of the specific parameters in Table S3, focusing only on the data for polycrystalline films, as they are the most relevant for high performance perovskite devices comparing to our high performance (FA,MA)Pb(I,Br)₃ perovskite:

- (1) Mobilities (hole and electron): range from 2-70 cm²/Vs and our CRPH study yields 7-28 cm²/Vs, which overlaps with most reports.
- (2) Equilibrium carrier densities: range from 10⁹ /cm³ to 6×10¹⁴ /cm³; the wide variation could be due to different compositions for the samples. For the high performance (FA,MA)Pb(I,Br)₃ samples considered in this study, for example, we have low carrier density of ~10¹² /cm³, within the range of other measurements.
- (3) Lifetime (τ): ranges from 10 - 36,000 ns, which overlaps favorably with our CRPH results (44 - 40,000 ns). In light of the new understanding generated from our CRPH analysis, such wide variation is to be expected given variation in light or carrier injection level for the measurements. The higher the light intensity (or carrier density) the lower the lifetime is, as the system operates in different recombination regimes. Therefore, as we noted in the main text, it is very important when reporting lifetime values to indicate the absorbed photon density level, G_γ (or, if possible, the excess carrier density, Δn).
- (4) Carrier diffusion length (L_D): ranges from 0.1-230 μ m, which overlaps favorably with our CRPH results (1.7-34 μ m). The situation is similar to lifetime in that the values vary significantly with light intensity and, from our CRPH analysis, such wide variation is to be expected due to variation in light or carrier injection level. Therefore, again, it is important to indicate G_γ , or if possible Δn , in reporting L_D .
- (5) The monomolecular recombination coefficient k_1 : ranges from 10⁶ to 10⁹ /s, while our CRPH analysis yields a lower value of $k_1=2.5\times10^4$ /s. The lower value implies a very long lifetime τ in the monomolecular regime, which could be due to very low trap density and indicative of the high material quality.

G. Summary of Recent Kesterite Transport Studies

Table S4. Summary of recent electrical transport studies for kesterites. The result from the current carrier-resolved photo-Hall effect study is highlighted in yellow. A study on the 12.6% PCE champion CZTSSe is reported in Row#14 (in bold).

No	Refs	Material	Type	Techniques	Lifetime (ns)	Diffusion Length (μm)		Mobility (cm ² /Vs)		Carrier conc. (/cm ³)	
						Electron	Hole	Electron	Hole	Electron	Hole
1	[52]	CZTSe	pc	TR-PL	7-9						
2	[53]	CZTSSe	pc	TR-PL, Drive-level capacitance profiling (DLCP)	3.1						8x10 ¹⁵
3	[54]	CZTSSe	pc	TR-PL	10						
4	[55]	CZTSSe	pc	DLCP							(0.2-1.5)x10 ¹⁶
5	[56]	CZTSe	sc	Hall effect					40-55		1x10 ¹⁷
6	[57]	CZTSSe	pc	TR-PL	6.7±1.4						
7	[14]	CZTSSe	pc	TR-PL, EQE, reflectance measurement, capacitance-voltage (C-V) measurement	1.5-15	0.3-1.2		11-257			
8	[58]	CZTSSe	pc	TR-PL	5						
9	[59]	CZTS	pc	TR-PL, DLCP	7.8	~0.35					1x10 ¹⁶
10	[60]	CZTS	pc	TR-PL	18.4						
		CZTSe	pc		9.3						
11	[61]	CZTSe	pc	Hall effect					1.23		2x10 ¹⁷
12	[62]	CZTSSe	pc	C-V							(1-4)x10 ¹⁶
13	[63]	CZTS	pc	Hall effect							(4.9-6.9)x10 ¹⁵
14	[38]	CZTSSe	pc	C-V, DLCP, QE, EBIC (PCE 12.6% champion)	0.75±0.15						8x10 ¹⁵
15	[64]	CZTSe	pc	DLCP, QE, reflectance measurement, TR-PL	2-2.5	2.1±0.5		690			2x10 ¹⁵
16	[18]	CZTSSe	pc	Hall effect (ac/PDL)				0.3-0.4			(1.6-2.2)x10 ¹⁶
17	[65]	CZTSe	pc	TR-PL, DLCP	4.2						~10 ¹⁶
18	[66]	CZTSe	pc	Hall effect				0.2-0.5			(2-20)x10 ¹⁶
19	[67]	CZTSe	sc	Hall effect				50-150			10 ¹⁷ -10 ¹⁹
20	[68]	CZTSSe	pc	TR-PL	8.1						
21	[69]	CZTSSe	pc	TR-PL	2.6						
		CZTGeSSe	pc		10						
22	[70]	CZTSe	pc	TR-PL	2.4						
		AgCZTSe	pc		3.6-10						
23	[71]	CZTSSe	pc	Hall				0.5-1.3			(1.4-19)x10 ¹⁵
24	[72]	CZTSe	pc	Hall effect (ac/PDL), DLCP				0.2			1x10 ¹⁶
		AgCZTSe	pc					0.2-1.1			10 ¹³ -10 ¹⁶
25	[73]	CZTSe	pc	TR-PL	1.3-2.2						
26	[74]	CZTS	pc	TR-PL, C-V	5.8-12.4						(3-5)x10 ¹⁶
27	[75]	CZTSSe	pc	C-V							(1-2)x10 ¹⁶
28	[76]	CZTS	pc	TR-PL, DLCP	4.1						4.4x10 ¹⁶
		CZCTS	pc		10.8						1.4x10 ¹⁶
29	[77]	CZTS	pc	TR-PL, C-V	10	~0.35					3x10 ¹⁶
30	[78]	CZTSe	pc	TR-PL, C-V	1.6						1.5x10 ¹⁶
31	[79]	CZTSSe	pc	Hall effect (ac/PDL)					0.3		1x10 ¹⁵
32	[80]	CZTSe	pc	TR-PL, C-V	1-8						10 ¹⁵ -10 ¹⁸
33		CZTSSe	pc	Carrier-resolved photo-Hall effect	23-66	0.7-1.5	0.23-0.42	9.0±0.1	0.9±0.1	$\Delta n(G_\gamma)$	1.6x10 ¹⁵
				Values are mapped against G_γ or Δn (Fig. 3) (IBM/KAIST/KRICT)	$\tau(G_\gamma)$	$L_{D,N}(G_\gamma)$	$L_{D,P}(G_\gamma)$	$\mu_n(G_\gamma)$	$\mu_p(G_\gamma)$	$\Delta n(G_\gamma)$	$\mu_0 + \Delta n(G_\gamma)$

Notes: (1) pc = poly crystalline, sc = single crystal

In Table S4, the CZTSSe samples studied offer a wide degree of variation in terms of compositions, e.g. S/(S+Se) ratio or metal ratio Cu/(Zn+Sn), fabrication methods and device performance levels (PCE~7%-12.6%). Some studies also use different alloys, such as AgCZTSe⁷².

Here we discuss some of the parameter variation, focusing only on the data for the polycrystalline films, since these yield the highest performance CZTSSe devices.

(1) Mobilities (hole): Range from 0.3 to 1.3 cm^2/Vs . The CZTSSe sample that we used in the current study is more recent and was exfoliated from the high performance device batch (see SI H) and prepared as a Hall sample, yielding mobility $\mu \sim 0.9 \text{ cm}^2/\text{Vs}$. From CRPH we obtain electron (minority) mobility, $\mu_N \sim 9 \text{ cm}^2/\text{Vs}$, significantly higher than that for holes and consistent with a theoretical study that suggests the hole effective mass in $\text{Cu}_2\text{ZnSn}(\text{S},\text{Se})_4$ should be larger than that for the electron (by as much as $4\times$)⁸¹.

(2) Equilibrium carrier densities: Range from 10^{15} /cm^3 to 10^{18} /cm^3 . Most variation of the density is due to varying S/(S+Se) and Cu/(Zn+Sn) ratios. Lower S content or higher Cu content leads to higher majority carrier (hole) density^{71,82}. C-V approaches tend to yield higher densities than those achieved with Hall effect, as they are sensitive to interface trap states at the edge of the space charge region³⁸. For the CZTSSe sample that we examined in the current study ($\text{S}/(\text{S}+\text{Se}) \approx 0.2$, $\text{Cu}/(\text{Zn}+\text{Sn}) \approx 0.8$ and $\text{Zn}/\text{Sn} \approx 1.1$), we have a hole density of $1.6 \times 10^{15} \text{ /cm}^3$, as measured by ac/PDL Hall technique.

(3) Lifetime (τ): Ranges from 1-18 ns, and has mostly been determined using time-resolved photoluminescence (TRPL), while our CRPH approach yields 23-66 ns. This discrepancy may at least in part be due to the light intensity or injection level used for these studies. The CRPH study operates in the low injection regime, with excess carrier density $\Delta n < 2 \times 10^{14} \text{ /cm}^3$, while the TRPL study uses a very high injection level, as much as $\Delta n \sim 10^{19} \text{ /cm}^3$ ⁸³, in order to attain sufficient PL signal due to the low radiative efficiency for CZTSSe.

(4) Minority carrier diffusion length ($L_{D,N}$): ranges from 0.3-2.1 μm , as measured by a combination of biased quantum efficiency and C-V measurement¹⁴, and 0.75 μm , as measured using the electron beam-induced-current mapping technique³⁸. These values overlap and are in agreement with our CRPH results: $L_{D,N} \sim (0.7\text{-}1.5) \mu\text{m}$.

H. Device fabrication and characteristics of Kesterite

The CZTSSe solar cell was prepared using a hydrazine-based pure solution approach that resulted in the 12.6% record efficiency as reported in ref. 38. The CdS emitter was deposited by chemical bath deposition (CBD) on the absorber layer. Transparent conductive oxide (ZnO/ITO) was sputter-deposited on the CdS. The electrical contact grid for the cell was made by evaporation (deposition area defined by a mask) of a thin layer of Ni followed by 2 μm of Al. A MgF₂ anti-reflective coating was deposited by evaporation. The finished device was then scribed to isolate the cell and the cell area was measured using a digital optical microscope ($A=0.453 \text{ cm}^2$).

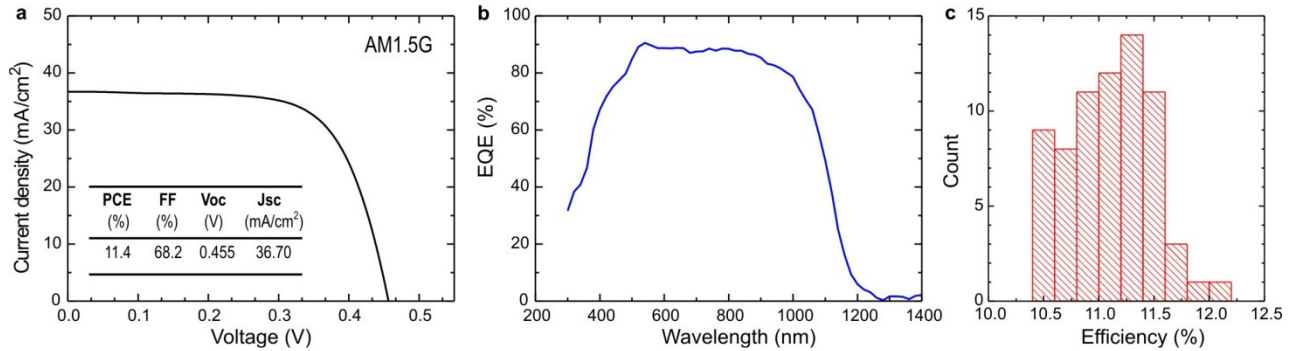


Figure S8. Device performance of the CZTSSe solar cell: (a) *J-V* curves under AM1.5G simulated light. The photovoltaic parameters are shown in the inset. (b) The EQE spectrum. (c) Histogram of the power conversion efficiencies obtained from 70 CZTSSe cells.

The device was measured using a solar simulator (Newport, Oriel Class A, 91192-1000) with simulated AM1.5G illumination of 100 mW/cm². We use a Si reference cell from Oriel (P/N 91150V) to calibrate the light intensity (calibrated by Newport, calibration#0847) and Keithley 2440 source meter for *I-V* measurement. The measurement was done in open air at ambient room temperature. The devices were soaked for about 30 sec at 1 sun prior to *I-V* measurement, and the measurement was performed with scan speed of approximately 2 V/s, all with a reverse scan direction (there is no noticeable hysteresis in the *I-V* traces). The characteristics of a high performing device from the same film as used for the photo-Hall study are shown in Fig. S8a. The device yields PCE = 11.4%, FF = 68.2%, Voc = 0.455 V and J_{SC} = 36.70 mA/cm². The external quantum efficiency (EQE) spectrum for the device is presented in Fig. S8b. Integrated current density of 40.0 mA/cm² from the EQE spectrum shows 9% higher than that (36.7 mA/cm²) measured under solar simulator. The bandgap determined from the inflection of EQE curve near the bandedge is Eg = 1.11 eV. A histogram of the efficiency of 70 CZTSSe samples from the same processing batch is shown in Fig. S8c, with overall average efficiency of (11.1 ± 0.4)%.

For photo-Hall study, the CZTSSe absorber layer was isolated from the blank area of a finished device after removing the top stack (CdS/ZnO/ITO/Ni/Al/MgF₂) by sonication in 10% aqueous HCl for 2 minutes and rinsing with water. Afterwards the absorber layer was exfoliated onto a secondary 5 mm × 5 mm glass substrate, from the underlying Mo/glass layer, using the method described in ref. 71. Then we deposited four terminal Ti/Au (10 nm/100 nm) square contacts on the four corners to define a Van der Pauw sample with area of 3 mm × 3 mm.

References:

31. Wang, Q. *et al.* Qualifying composition dependent *p* and *n* self-doping in CH₃NH₃PbI₃. *Appl. Phys. Lett.* **105**, 163508 (2014).
32. Chen, Y., Yi, H. T. & Podzorov, V. High-resolution ac measurements of the Hall effect in organic field-effect transistors. *Phys. Rev. Appl.* **5**, 034008 (2016).

33. McDonald, K. T. *Long Rod with Uniform Magnetization Transverse to its Axis*, <http://www.physics.princeton.edu/~mcdonald/examples/magrod.pdf>. (1999). Accessed June 5, 2019.

34. Smith, R. A. *Semiconductors*. 2nd edn, (Cambridge Univ. Press, Cambridge, 1978).

35. Duggan, G. & Scott, G. B. The efficiency of photoluminescence of thin epitaxial semiconductors. *J. Appl. Phys.* **52**, 407-411 (1981).

36. Cesaria, M., Caricato, A. & Martino, M. Realistic absorption coefficient of ultrathin films. *J. Optics* **14**, 105701 (2012).

37. de Quilettes, D. W. *et al.* Impact of microstructure on local carrier lifetime in perovskite solar cells. *Science* **348**, 683-686 (2015).

38. Wang, W. *et al.* Device characteristics of CZTSSe thin film solar cell with 12.6% efficiency. *Adv. Ener. Mater.* **4**, 1301465 (2014).

39. Zhao, Y., Nardes, A. M. & Zhu, K. Solid-state mesostructured perovskite $\text{CH}_3\text{NH}_3\text{PbI}_3$ solar cells: charge transport, recombination, and diffusion length. *J. Phys. Chem. Lett.* **5**, 490-494 (2014).

40. Oga, H., Saeki, A., Ogomi, Y., Hayase, S. & Seki, S. Improved understanding of the electronic and energetic landscapes of perovskite solar cells: high local charge carrier mobility, reduced recombination, and extremely shallow traps. *J. Am. Chem. Soc.* **136**, 13818-13825 (2014).

41. Bi, C. *et al.* Understanding the formation and evolution of interdiffusion grown organolead halide perovskite thin films by thermal annealing. *J. Mater. Chem. A* **2**, 18508-18514 (2014).

42. Saba, M. *et al.* Correlated electron-hole plasma in organometal perovskites. *Nat. Comm.* **5**, 5049 (2014).

43. Yamada, Y., Nakamura, T., Endo, M., Wakamiya, A. & Kanemitsu, Y. Photocarrier recombination dynamics in perovskite $\text{CH}_3\text{NH}_3\text{PbI}_3$ for solar cell applications. *J. Am. Chem. Soc.* **136**, 11610-11613 (2014).

44. Kedem, N. *et al.* Light-induced increase of electron diffusion length in a *p-n* junction type $\text{CH}_3\text{NH}_3\text{PbBr}_3$ perovskite solar cell. *J. Phys. Chem. Lett.* **6**, 2469-2476 (2015).

45. Rehman, W. *et al.* Charge-carrier dynamics and mobilities in formamidinium lead mixed-halide perovskites. *Adv. Mater.* **27**, 7938-7944 (2015).

46. Reid, O. G., Yang, M., Kopidakis, N., Zhu, K. & Rumbles, G. Grain-size-limited mobility in methylammonium lead iodide perovskite thin films. *ACS Ener. Lett.* **1**, 561-565 (2016).

47. Zhumekenov, A. A. *et al.* Formamidinium lead halide perovskite crystals with unprecedented long carrier dynamics and diffusion length. *ACS Ener. Lett.* **1**, 32-37 (2016).

48. Bi, Y. *et al.* Charge carrier lifetimes exceeding 15 μs in methylammonium lead iodide single crystals. *J. Phys. Chem. Lett.* **7**, 923-928 (2016).

49. Kiermasch, D., Rieder, P., Tvingstedt, K., Baumann, A. & Dyakonov, V. Improved charge carrier lifetime in planar perovskite solar cells by bromine doping. *Sci. Rep.* **6**, 39333 (2016).

50. Keshavarz, M. *et al.* Light- and Temperature-modulated magneto-transport in organic-inorganic lead halide perovskites. *ACS Ener. Lett.* **3**, 39-45 (2017).

51. Kim, D. H. *et al.* 300% enhancement of carrier mobility in uniaxial-oriented perovskite films formed by topotactic-oriented attachment. *Adv. Mater.* **29**, 1606831 (2017).

52. Shin, B., Zhu, Y., Bojarczuk, N. A., Chey, S. J. & Guha, S. Control of an interfacial MoSe_2 layer in $\text{Cu}_2\text{ZnSnSe}_4$ thin film solar cells: 8.9% power conversion efficiency with a TiN diffusion barrier. *Appl. Phys. Lett.* **101**, 053903 (2012).

53. Barkhouse, D. A. R., Gunawan, O., Gokmen, T., Todorov, T. K. & Mitzi, D. B. Device characteristics of a 10.1% hydrazine-processed $\text{Cu}_2\text{ZnSn}(\text{Se},\text{S})_4$ solar cell. *Prog. Photovolt: Res. Appl.* **20**, 6-11 (2012).

54. Bag, S. *et al.* Low band gap liquid-processed CZTSe solar cell with 10.1% efficiency. *Energy Environ. Sci.* **5**, 7060-7065 (2012).

55. Gunawan, O. *et al.* Electronic properties of the $\text{Cu}_2\text{ZnSn}(\text{Se},\text{S})_4$ absorber layer in solar cells as revealed by admittance spectroscopy and related methods. *Appl. Phys. Lett.* **100**, 253905 (2012).

56. Nagaoka, A., Yoshino, K., Taniguchi, H., Taniyama, T. & Miyake, H. Growth of $\text{Cu}_2\text{ZnSnSe}_4$ single crystals from Sn solutions. *J. Crystal Growth* **354**, 147-151 (2012).

57. Todorov, T. K. *et al.* Beyond 11% efficiency: Characteristics of state-of-the-art $\text{Cu}_2\text{ZnSn}(\text{S},\text{Se})_4$ solar cells. *Adv. Ener. Mater.* **3**, 34-38 (2013).

58. Gokmen, T., Gunawan, O., Todorov, T. K. & Mitzi, D. B. Efficiency limitation and band tailing in kesterite solar cells. *Appl. Phys. Lett.* **103**, 103506 (2013).

59. Shin, B. *et al.* Thin film solar cell with 8.4% power conversion efficiency using earth abundant $\text{Cu}_2\text{ZnSnS}_4$ absorber. *Prog. Photovolt: Res. Appl.* **21**, 72 (2013).

60. Guo, L. *et al.* Electrodeposited $\text{Cu}_2\text{ZnSnSe}_4$ thin film solar cell with 7% power conversion efficiency. *Prog. Photovolt: Res. Appl.* **22**, 58-68 (2013).

61. Kuo, D.-H. & Tsega, M. Electrical conduction and mobility enhancement in *p*-type In-doped $\text{Cu}_2\text{ZnSnSe}_4$ bulks. *Jpn. J. Appl. Phys.* **53**, 035801 (2014).

62. Kim, J. *et al.* High efficiency $\text{Cu}_2\text{ZnSn}(\text{S},\text{Se})_4$ solar cells by applying a double $\text{In}_2\text{S}_3/\text{CdS}$ emitter. *Adv. Mat.* **26**, 7427-7431 (2014).

63. Courel, M., Vigil-Galán, O., Jiménez-Olarte, D., Espíndola-Rodríguez, M. & Saucedo, E. Trap and recombination centers study in sprayed $\text{Cu}_2\text{ZnSnS}_4$ thin films. *J. Appl. Phys.* **116**, 134503 (2014).

64. Lee, Y. S. *et al.* $\text{Cu}_2\text{ZnSnSe}_4$ thin-film solar cells by thermal co-evaporation with 11.6% power conversion efficiency and improved minority carrier diffusion length. *Adv. Ener. Mater.* **5**, 1401372 (2015).

65. Ben Messaoud, K. *et al.* Impact of the Cd_{2+} treatment on the electrical properties of $\text{Cu}_2\text{ZnSnSe}_4$ and $\text{Cu}(\text{In},\text{Ga})\text{Se}_2$ solar cells. *Prog. Photovolt: Res. Appl.* **23**, 1608-1620 (2015).

66. Gershon, T. *et al.* The impact of sodium on the sub-bandgap states in CZTSe and CZTS. *Appl. Phys. Lett.* **106**, 123905 (2015).

67. Bishop, D. M., McCandless, B. E., Haight, R., Mitzi, D. B. & Birkmire, R. W. Fabrication and electronic properties of CZTSe single crystals. *IEEE J. Photovolt.* **5**, 390-394 (2015).

68. Haass, S. G. *et al.* 11.2% efficient solution processed kesterite solar cell with a low voltage deficit. *Adv. Ener. Mat.* **5**, 1500712 (2015).

69. Hages, C. J. *et al.* Improved performance of Ge-alloyed CZTGeSSe thin-film solar cells through control of elemental losses. *Prog. Photovolt.: Res. Appl.* **23**, 376-384 (2015).

70. Hages, C. J., Kooper, M. J. & Agrawal, R. Optoelectronic and material properties of nanocrystal-based CZTSe absorbers with Ag-alloying. *Sol. En. Mat. Solar Cells* **145**, 342-348 (2016).

71 Tai, K. F. *et al.* Fill factor losses in $\text{Cu}_2\text{ZnSn}(\text{S}_x\text{Se}_{1-x})_4$ solar cells: Insights from physical and electrical characterization of devices and exfoliated films. *Adv. Ener. Mater.* **6**, 1501609 (2015).

72 Gershon, T. *et al.* Photovoltaic materials and devices based on the alloyed kesterite absorber $(\text{Ag}_x\text{Cu}_{1-x})_2\text{ZnSnSe}_4$. *Adv. Ener. Mater.* **6**, 1502468 (2016).

73 Li, J. *et al.* Growth of $\text{Cu}_2\text{ZnSnSe}_4$ film under controllable Se vapor composition and impact of low Cu content on solar cell efficiency. *ACS Appl. Mat. Interfaces* **8**, 10283-10292 (2016).

74 Liu, F. *et al.* Nanoscale microstructure and chemistry of $\text{Cu}_2\text{ZnSnS}_4/\text{CdS}$ interface in kesterite $\text{Cu}_2\text{ZnSnS}_4$ solar cells. *Adv. Ener. Mater.* **6**, 1600706 (2016).

75 Yang, K.-J. *et al.* A band-gap-graded CZTSSe solar cell with 12.3% efficiency. *J. Mat. Chem. A* **4**, 10151-10158 (2016).

76 Yan, C. *et al.* Beyond 11% efficient sulfide kesterite $\text{Cu}_2\text{Zn}_x\text{Cd}_{1-x}\text{SnS}_4$ solar cell: Effects of cadmium alloying. *ACS Ener. Lett.* **2**, 930-936 (2017).

77 Cazzaniga, A. *et al.* Ultra-thin $\text{Cu}_2\text{ZnSnS}_4$ solar cell by pulsed laser deposition. *Sol. Ener. Mat. Sol. Cells* **166**, 91-99 (2017).

78 Tampo, H., Kim, K. M., Kim, S., Shibata, H. & Niki, S. Improvement of minority carrier lifetime and conversion efficiency by Na incorporation in $\text{Cu}_2\text{ZnSnSe}_4$ solar cells. *J. Appl. Phys.* **122**, 023106 (2017).

79 Lie, S. *et al.* Reducing the interfacial defect density of CZTSSe solar cells by Mn substitution. *J. Mat. Chem. A* **6**, 1540-1550 (2018).

80 Haass, S. G. *et al.* Complex interplay between absorber composition and alkali doping in high-efficiency kesterite solar cells. *Adv. Ener. Mater.* **8**, 1701760 (2017).

81 Persson, C. Electronic and optical properties of $\text{Cu}_2\text{ZnSnS}_4$ and $\text{Cu}_2\text{ZnSnSe}_4$. *J. Appl. Phys.* **107**, 053710 (2010).

82 Gunawan, O., Gokmen, T. & Mitzi, D. B. Suns-Voc characteristics of high performance kesterite solar cells. *J. Appl. Phys.* **116**, 084504 (2014).

83 Tai, K. F., Gershon, T., Gunawan, O. & Huan, C. H. A. Examination of electronic structure differences between CIGSSe and CZTSSe. *J. Appl. Phys.* **117**, 235701 (2015).